Modulation of Coordinated Activity across Cortical Layers by Plasticity of Inhibitory Synapses

Joana Lourenço, Angela Michela de Stasi, Charlotte Deleuze, Mathilde Bigot, Antonio Pazienti, Andrea Aguirre, Michele Giugliano, Srdjan Ostojic, Alberto Bacci

▶ **To cite this version:**

Joana Lourenço, Angela Michela de Stasi, Charlotte Deleuze, Mathilde Bigot, Antonio Pazienti, et al.. Modulation of Coordinated Activity across Cortical Layers by Plasticity of Inhibitory Synapses. Cell Reports, 2020, 30 (3), pp.630-641. 10.1016/j.celrep.2019.12.052 . hal-02473284

HAL Id: hal-02473284

https://hal.sorbonne-universite.fr/hal-02473284

Submitted on 10 Feb 2020

HAL is a multi-disciplinary open access archive for the deposit and dissemination of scientific research documents, whether they are published or not. The documents may come from teaching and research institutions in France or abroad, or from public or private research centers.

L'archive ouverte pluridisciplinaire **HAL**, est destinée au dépôt et à la diffusion de documents scientifiques de niveau recherche, publiés ou non, émanant des établissements d'enseignement et de recherche français ou étrangers, des laboratoires publics ou privés.

Article

Cell Reports

Modulation of Coordinated Activity across Cortical Layers by Plasticity of Inhibitory Synapses

Graphical Abstract

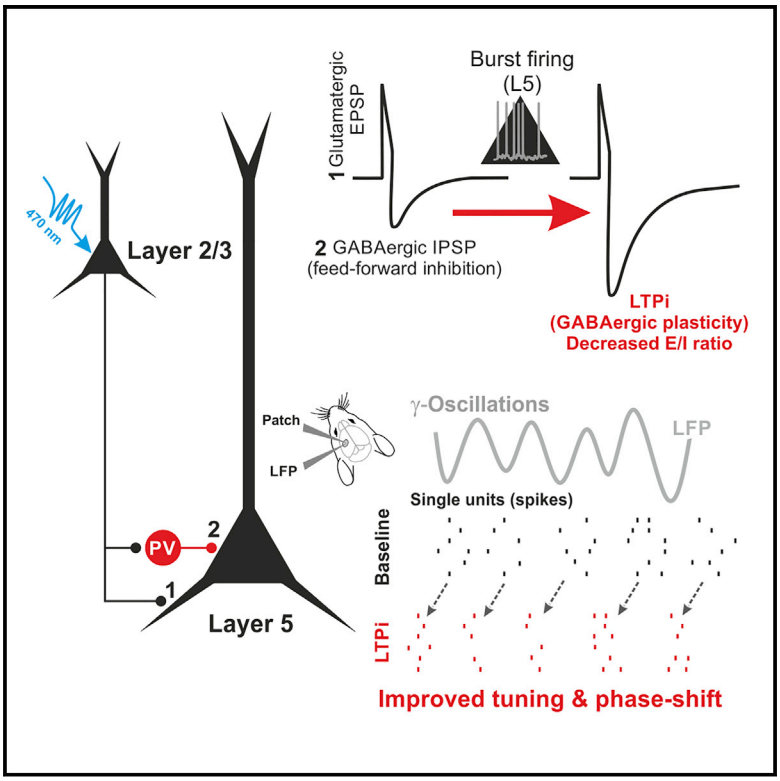

Highlights

- Feedforward inhibition (FFI) of layer 5 pyramidal neurons (PNs) is highly plastic
- Long-term potentiation of FFI modulates spiking activity of layer 5 PNs
- LTPi affects information transfer across cortical layers
- The strength of LTPi determines the phase locking of PN firing to γ-oscillations

Authors

Joana Lourenço, Angela Michela De Stasi, Charlotte Deleuze, ..., Michele Giugliano, Srdjan Ostojic, Alberto Bacci

Correspondence

joana.lourenco@icm-institute.org (J.L.), alberto.bacci@icm-institute.org (A.B.)

In Brief

Lourenço et al. demonstrate that burst firing of layer 5 pyramidal neurons (PNs) induces long-term potentiation of inhibition (LTPi). LTPi strongly affects PN input/output spikes, prevents transfer of information across cortical layers, and affects phase locking of PN firing to cognition-relevant rhythmic activity.

Lourenço et al., 2020, Cell Reports *30*, 630–641
January 21, 2020 © 2019 The Authors.
https://doi.org/10.1016/j.celrep.2019.12.052

CellPress

OPEN ACCESS
CellPress

Cell Reports
Article

Modulation of Coordinated Activity across Cortical Layers by Plasticity of Inhibitory Synapses

Joana Lourenço,[1,*] Angela Michela De Stasi,[1] Charlotte Deleuze,[1] Mathilde Bigot,[2] Antonio Pazienti,[3,5] Andrea Aguirre,[1] Michele Giugliano,[4] Srdjan Ostojic,[2] and Alberto Bacci[1,6,*]

[1]Institut du Cerveau et de la Moelle Épinière (ICM), CNRS UMR 7225, INSERM U1127, Sorbonne Université, 75013 Paris, France
[2]Laboratoire de Neurosciences Cognitives, INSERM U960, Ecole Normale Supérieure, PSL Research University, 75005 Paris, France
[3]European Brain Research Institute, Fondazione Rita Levi-Montalcini, 00143 Rome, Italy
[4]Department of Biomedical Sciences and Institute Born-Bunge, Molecular, Cellular, and Network Excitability, Universiteit Antwerpen, Antwerpen, Belgium
[5]Present address: Istituto Superiore di Sanità, 00161 Rome, Italy
[6]Lead Contact
*Correspondence: joana.lourenco@icm-institute.org (J.L.), alberto.bacci@icm-institute.org (A.B.)
https://doi.org/10.1016/j.celrep.2019.12.052

SUMMARY

In the neocortex, synaptic inhibition shapes all forms of spontaneous and sensory evoked activity. Importantly, inhibitory transmission is highly plastic, but the functional role of inhibitory synaptic plasticity is unknown. In the mouse barrel cortex, activation of layer (L) 2/3 pyramidal neurons (PNs) elicits strong feedforward inhibition (FFI) onto L5 PNs. We find that FFI involving parvalbumin (PV)-expressing cells is strongly potentiated by postsynaptic PN burst firing. FFI plasticity modifies the PN excitation-to-inhibition (E/I) ratio, strongly modulates PN gain, and alters information transfer across cortical layers. Moreover, our LTPi-inducing protocol modifies firing of L5 PNs and alters the temporal association of PN spikes to γ-oscillations both *in vitro* and *in vivo*. All of these effects are captured by unbalancing the E/I ratio in a feedforward inhibition circuit model. Altogether, our results indicate that activity-dependent modulation of perisomatic inhibitory strength effectively influences the participation of single principal cortical neurons to cognition-relevant network activity.

INTRODUCTION

In the neocortex, sensory integration is accomplished through the coordinated activity of neuronal networks across different cortical layers and columns (reviewed in Allene et al., 2015; Douglas et al., 2004; Feldmeyer, 2012). These hardwired anatomical connectivity patterns between several neuron types define specific pathways and enable salient flow of information across and within different cortical layers.

Functional cortical networks result from direct contact between neurons and indirect feedforward and feedback connections from intercalated neurons, whose recruitment strength and excitability contribute to the formation and dissolution of neuronal ensembles (Buzsáki, 2010). These interposed neurons are mostly (but not only) inhibitory. Importantly, fast synaptic inhibition plays a fundamental role in shaping and sculpting virtually all forms of cortical activity (Atallah et al., 2012; Buzsáki and Wang, 2012; Cardin et al., 2009; Lee et al., 2012; Sachdev et al., 2012; Sohal et al., 2009; Tremblay et al., 2016; Veit et al., 2017; Wilson et al., 2012).

Neocortical inhibition is provided by a rich diversity of GABAergic interneurons (Ascoli et al., 2008; Kepecs and Fishell, 2014; Méndez and Bacci, 2011). In particular, parvalbumin (PV)-positive, perisomatic targeting interneurons account for nearly half of all cortical inhibitory cells (Bodor et al., 2005; Freund and Katona, 2007). Perisomatic inhibition from PV cells exerts a plethora of functions within neocortical circuits, including control of pyramidal neuron (PN) output activity and gain during sensory perception (Atallah et al., 2012; Carandini and Heeger, 2011; Lee et al., 2012; Silver, 2010; Wilson et al., 2012) and the ability to drive fast cortical oscillations underlying several aspects of cognition (Bartos et al., 2007; Buzsáki and Silva, 2012; Cardin et al., 2009; Isaacson and Scanziani, 2011; Sohal et al., 2009; Wang, 2010), thus likely acting as a synchronizing mechanism and likely promoting the generation of cell assemblies (Buzsáki, 2010).

PV cell-mediated perisomatic inhibition equalizes excitation proportionally, resulting in a tight balanced excitation-to-inhibition (E/I) ratio in single PNs (Atallah and Scanziani, 2009; Xue et al., 2014). Notably, perturbation of PN activity *in vivo* has been shown to modify PV-mediated perisomatic GABAergic inhibition (Xue et al., 2014). We have found that postsynaptic depolarization or bursts of action potentials in layer (L) 5 PNs of the mouse barrel cortex induces long-term potentiation of inhibition (LTPi), which is selective for PV cell transmission and sharpens the time window of synaptic integration (Lourenço et al., 2014).

In the last four decades, long-term plasticity of synaptic transmission has been studied extensively at glutamatergic synapses because it is considered the cellular correlate of learning and memory (Malenka, 2003). Importantly, inhibitory synapses are also highly plastic (Castillo et al., 2011; Chiu et al., 2018, 2019;

 © 2019 The Authors.
This is an open access article under the CC BY-NC-ND license (http://creativecommons.org/licenses/by-nc-nd/4.0/).

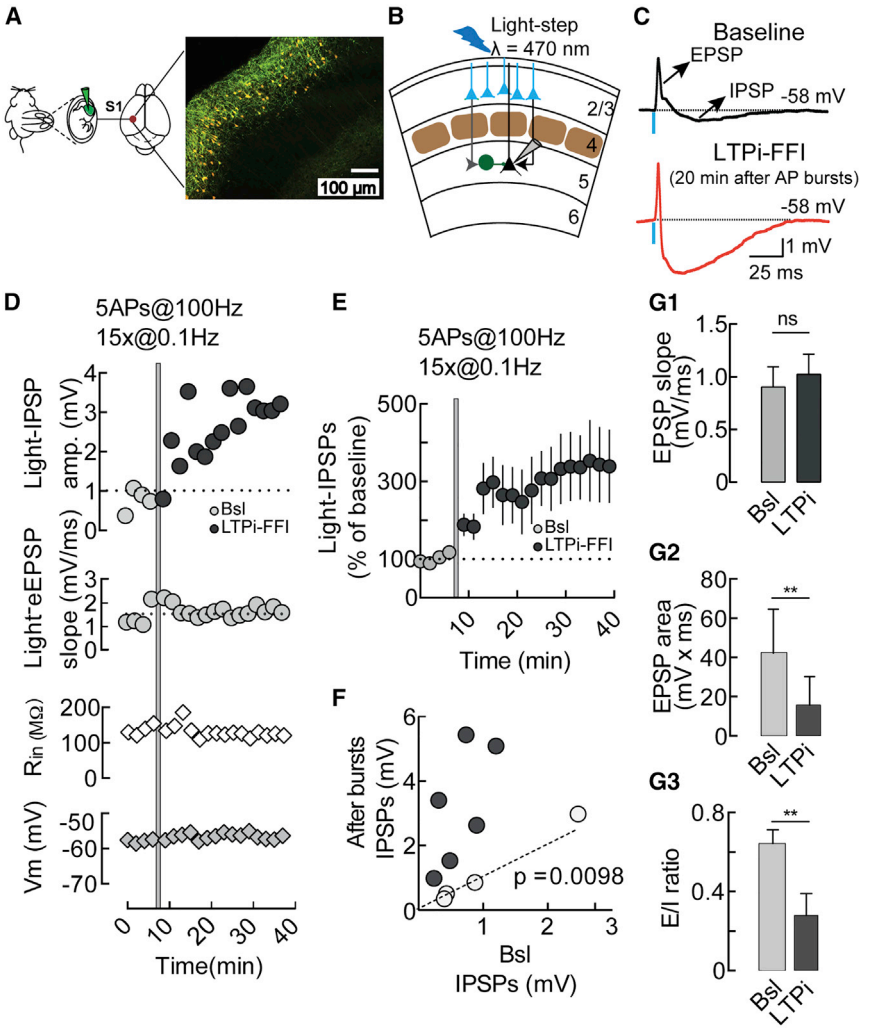

Figure 1. Burst Firing of L5 PNs Selectively Potentiates Feedforward GABAergic Input

(A) *In utero* electroporation of ChR2 and red fluorescent protein (RFP) in L2/3 PNs of the mouse S1.

(B) Scheme of the recording configuration.

(C) Average (10 sweeps) current-clamp traces of the EPSP-IPSP composite response recorded in L5 PNs upon photostimulation of L2/3 PNs before (black, top) and after (bottom, red) inducing LTPi.

(D) LTPi of light-IPSPs (top graph) of the cell shown in (C). The bottom graphs indicate light-EPSP slope, input resistance (Rin), and resting membrane potential (Vm) of the same cell.

(E) Population graph of LTPi in L5 PNs.

(F) Plot illustrating the relative change of light-IPSPs in response to burst firing of individual PNs (after 20 min). Dark circles, LTPi-expressing PNs; light gray circles, PNs not expressing LTPi; Bsl, baseline.

(G) Graphs showing average depolarizing slopes, areas, and the EPSP/IPSP ratio of composite PSPs in Bsl and after postsynaptic bursts. In some cases, the error bars are too small to be visible. n.s., not significant. *p < 0.05, **p < 0.01, with paired t test.

Population data are illustrated as mean ± SEM.

RESULTS

Burst Firing of L5 PNs Selectively Potentiates Feedforward GABAergic Inputs

L2/3 PNs play a prominent role in activating deep cortical output layers. We have demonstrated previously that bursts of action potentials (APs) in L5 PNs induce LTPi selectively at synapses from PV cells (Lourenço et al., 2014). We therefore asked whether L2/3 activation triggers PV cell-mediated FFI onto L5 PNs and whether this is plastic.

Using *in utero* electroporation, we expressed the light-sensitive opsin channelrhodospin 2 (ChR2) in a large fraction of L2/3 PNs (Figure 1A). We then performed whole-cell patch-clamp recordings from large L5 PNs in acute slices of the barrel cortex (S1, barrel field) from mice that had been electroporated previously *in utero* (Figures 1A and 1B). Brief (1-ms) stimulation with blue light (λ = 470 nm) of L2/3 ChR2+ PNs induced a composite postsynaptic potential (PSP) in L5 PNs recorded in current clamp mode. This composite PSP was made of an early excitatory PSP (EPSP) triggered by L2/3 PNs (Figure S1), which was followed by a GABAergic inhibitory PSP (IPSP; Figures 1B and 1C, top panel; Figure S1). This inhibitory component had typical disynaptic latencies (Figure S1) and was likely triggered by perisomatically targeting PV cells. Indeed, activation of L2/3 PNs recruited L5 PV interneurons efficiently (Figure S1; Kruglikov and Rudy, 2008; Mateo et al., 2011; Deleuze et al., 2019), and late GABAergic responses recorded in voltage-clamp had rise time values compatible with light-evoked synaptic events mediated by PV cells (Figures S1G and S1H; Lourenço et al., 2014).

Garkun and Maffei, 2014; Griffen and Maffei, 2014; Kurotani et al., 2008; Méndez and Bacci, 2011; Petrini et al., 2014; Vickers et al., 2018), but the functional role of GABAergic plasticity is unknown (but see Mongillo et al., 2018; Vogels et al., 2011).

Here we set out to investigate how the plasticity of PV cell-mediated perisomatic GABAergic synapses modulates several computations performed by single L5 PNs of the mouse barrel cortex (S1). Using *in utero* electroporation, we expressed light-sensitive opsins in L2/3 PNs of the mouse S1. We demonstrate that activation of L2/3 induces robust feedforward inhibition (FFI) on L5 PNs, mostly mediated by PV basket cells (Kruglikov and Rudy, 2008; Mateo et al., 2011). FFI could be strongly potentiated by cell-autonomous postsynaptic paradigms. LTPi-FFI modified the input/output relationship of L5 PNs and strongly modulated information flow across cortical layers. Moreover, LTPi-inducing bursts affected the temporal association of PN spiking with γ-oscillations both *in vitro* and *in vivo*. These results were captured by a computational model, indicating that plasticity of PV cell-dependent perisomatic inhibition can strongly modulate single PNs at the single-cell and network levels.

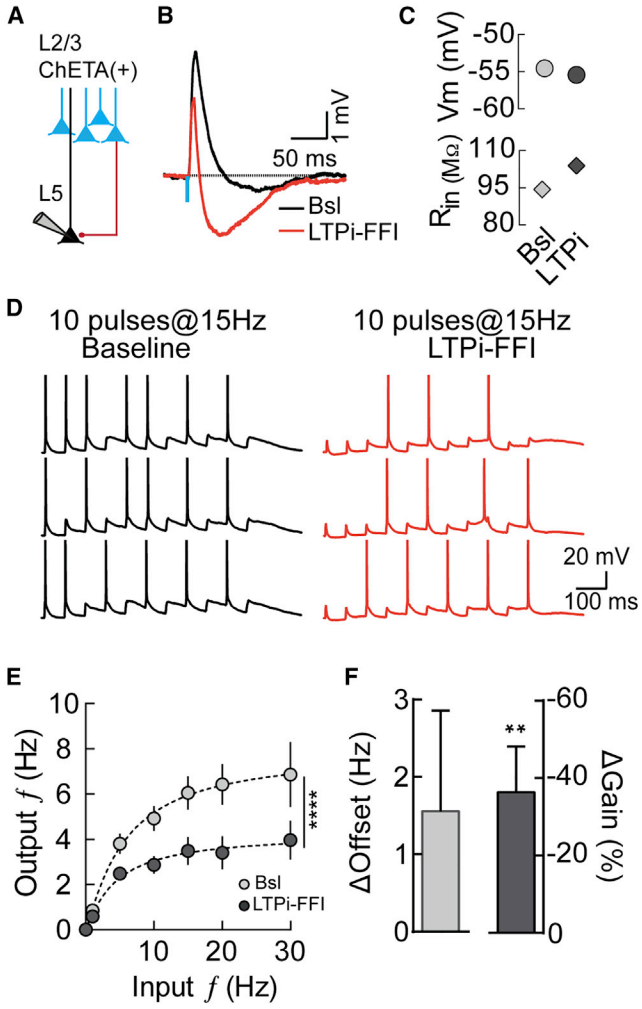

Figure 2. LTPi-FFI Induces a Multiplicative Gain Modulation of PN Output Spiking

(A) Schematic of the recording configuration.

(B) Averaged (10 sweeps) current-clamp traces of EPSP-IPSP responses in L5 PNs upon photostimulation of ChETA+ L2/3 PNs before (black) and after (red) LTPi induction.

(C) Vm (left panel) and Rin (right panel) throughout the experiment.

(D) Spiking output of L5 PNs upon photostimulation of L2/3 PNs at 15-Hz frequency during Bsl and after LTPi-FFI (red trace).

(E) Averaged output firing rate of L5 PNs upon photostimulation of L2/3 PNs at different frequencies before (Bsl, light gray) and 15 min after LTPi induction (LTPi-FFI, dark gray); ****$p < 0.0001$, Friedman test. Dashed lines are fits to a Hill function.

(F) Offset (light gray) and gain (dark gray) changes in the I/O function after LTPi-FFI from the fit in (D) (**$p < 0.01$, Wilcoxon matched-pairs signed-rank test, theoretical median = 0).

Population data are illustrated as mean ± SEM.

Importantly, in response to postsynaptic AP bursts of L5 PNs (5 APs at 100 Hz, repeated 15 times every 10 s), we observed an increase in amplitude of the GABAergic component of the light-evoked PSP (light-IPSP) that persisted for more than 30 min (Figures 1C–1F), which we termed long-term potentiation of feedforward inhibition (LTPi-FFI). LTPi-FFI was observed in ~65% of the recorded PNs (Figure S1I, includes all cells tested for LTPi-FFI in Figures 1, 2, and 4), and it induced an increase in light-IPSPs amplitude of at least 50% of the baseline amplitude (0.73 ± 0.2 versus 2.38 ± 0.58 mV, light-IPSP baseline versus 20 min after AP bursts, respectively; n = 10, p = 0.0098, Wilcoxon matched-pairs signed-rank test; Figure 1F; Figure S3A). We reported previously that this form of cell-autonomous plasticity is sensitive to retrograde nitric oxide (NO). Moreover, NO-mediated plasticity was expressed at PV-PN but not somatostatin (SST) interneuron-PN synapses (Lourenço et al., 2014). Likewise, LTPi-FFI was also sensitive to pharmacological inhibition of the canonical NO receptor guanylylcyclase (GC) with 1H-{1,2,4}oxadiazolo{4,3-a}quinoxalin-&-dione (ODQ, 10 μM; 0.73 ± 0.16 versus 0.89 ± 0.31 mV, light-IPSP baseline versus 20 min after AP bursts, respectively, in the continuous presence of ODQ; n = 8, p = 0.74, Wilcoxon matched-pairs signed-rank test; Figures S1J and S1K). Importantly, LTPi-FFI did not affect the slope of the depolarizing EPSP component (baseline, 0.904 ± 0.19 mV/ms; LTPi, 1.024 ± 0.0.19 mV, n = 10, p = 0.16, Wilcoxon matched-pairs signed-rank test; Figures 1D and 1G1). However, because of the potentiation of the hyperpolarizing (IPSP) component, the area of the light-evoked EPSP decreased significantly (baseline, 42.46 ± 7.47 mV/ms; LTPi, 15.73 ± 4.8 mV/ms; n = 10, p = 0.0036, paired t test; Figure 1G2). Consequently, LTPi-FFI strongly reduced the E/I ratio, measured as the EPSP area divided by the total composite PSP area (0.64 ± 0.07 versus 0.28 ± 0.11, baseline versus LTPi; n = 10, p = 0.0023, paired t test; Figure 1G3). In the presence of the NO receptor inhibitor ODQ, postsynaptic AP bursts failed to induce changes in the E/I ratio (0.79 ± 0.28 versus 0.636 ± 0.1 mV, baseline versus 20 min after AP bursts, in the continuous presence of ODQ; n = 8, p = 0.12, Wilcoxon matched-pairs signed-rank test; Figure S1L).

In sum, FFI onto L5 PNs was triggered by L2/3 PNs and could be strongly potentiated by postsynaptic firing activity alone. This form of plasticity was mediated by NO signaling and is thus consistent with the involvement of PV cells (Lourenço et al., 2014). Plasticity of FFI resulted in prolonged changes of the E/I balance in L5 PNs.

LTPi-FFI Induces a Divisive Gain Modulation of PN Output Spiking

Inhibitory transmission alters the computations performed by PNs, strongly affecting their input/output (I/O) relationship (Carandini and Heeger, 2011; Silver, 2010), but how plastic changes of inhibitory synaptic strength could modulate I/O is unknown. To address this question, we measured the I/O relationship before and after inducing LTPi-FFI in L5 PNs by postsynaptic AP bursts (Figures 2A–2C). To reliably evoke presynaptic spike trains, we expressed the fast light-sensitive opsin ChETA in L2/3 PNs via *in utero* electroporation. We then tested its effectiveness by recording spike activity in ChETA-expressing L2/3 PNs in response to trains of brief blue light pulses over a range of different frequencies (Figures S4A–S4C). *In utero* electroporated L2/3 PNs linearly followed ChETA stimulation at frequencies up to 30 Hz (Figure S2). The effect of LTPi-FFI on synaptic integration was then investigated by stimulating L2/3 ChETA(+) neurons with 10 pulses of light at different frequencies and measuring the

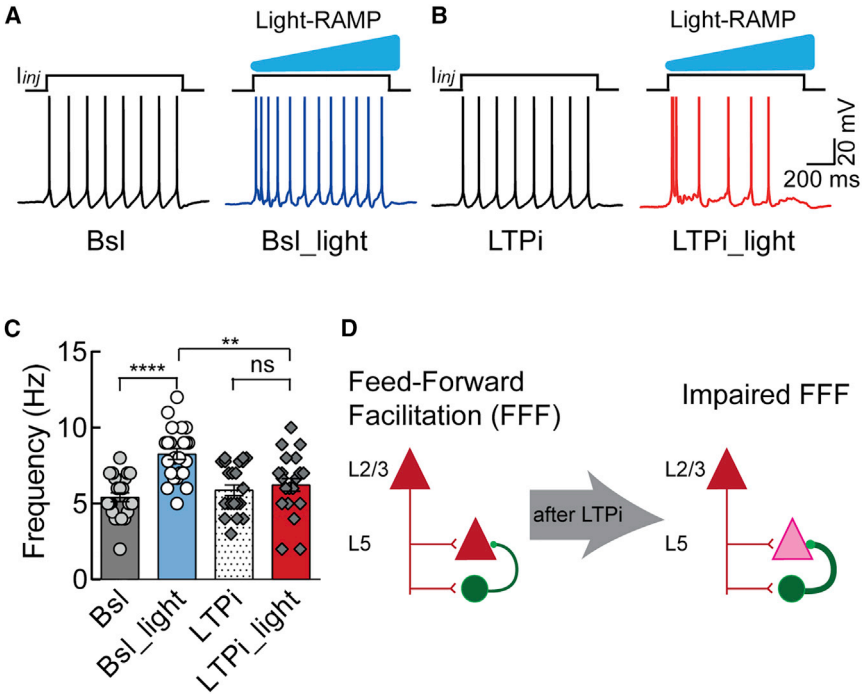

Figure 3. LTPi-FFI Affects the Flow Information across Cortical Layers

(A) Response of a L5 PN to a depolarizing current injection (+70 pA) under Bsl conditions without (left trace, Bsl) and with light stimulation (right trace, Bsl_light), inducing feedforward facilitation (FFF).

(B) The same cell as in (A) upon LTPi-inducing AP bursts. APs were clipped for display purposes.

(C) Average population data of FFF during Bsl conditions in the absence and presence of light (circles) and upon LTPI-FFI (diamonds, ****$p < 0.0001$) and Bsl_light and LTPi-FFI light conditions (**$p < 0.001$, Friedman test).

(D) Summary scheme of the effect of LTPi in preventing FFF across cortical layers. In the absence of LTPi, L2/3 activity efficiently spreads to L5 (left). LTPi prevents this prominent information transfer from L2/3 to L5 PNs.

Population data are illustrated as mean ± SEM.

mean output firing rate of L5 PNs (Figures 2D and 2E) before and after inducing LTPi-FFI. We observed an overall difference between baseline and LTPi-FFI with a major effect on higher frequencies between 15 and 30 Hz ($F_{(11,165)} = 13.76$, $p < 0.0001$; $p < 0.05$ for 15 Hz, $p < 0.0001$ for 20 Hz, and $p < 0.05$ for 30 Hz; Friedman test followed by Dunn's multiple comparison test; Figure 2E). The I/O relationship was quantified by fitting the data to Hill-like equations, which allowed us to extract slope and offset of I/O curves (Murphy and Miller, 2003; Rothman et al., 2009). We observed a shift in the input frequency required to achieve half maximum of the output frequency, although this was not significantly different ($\Delta_{Offset} = 1.56 \pm 1.3$ Hz, n = 14, p = 0.8, Wilcoxon matched-pairs signed-rank test, theoretical median = 0; Figure 2F, light gray bar). Despite an absence of significant changes in the subtractive shift behavior of the I/O curve, we observed a significant change in the slope ($\Delta_{Gain} = -36.29\% \pm 11.79\%$, n = 14, p = 0.01, Wilcoxon matched-pairs signed-rank test, theoretical median = 0; Figure 2F, dark gray bar). Importantly, in the minority of L5 PNs that failed to express LTPi-FFI (Figure S1I), we did not observe any change in gain modulation (Figure S2D). Thus, these results indicate that LTPi-FFI has as an almost purely divisive effect on the PN I/O relationship (Figures 2E and F).

LTPi-FFI Affects the Flow of Information across Cortical Layers

Sustained firing of L2/3 PNs induces lateral suppression of superficial cortical layers and simultaneously activates L5 PNs within the same column. This latter phenomenon is known as feedforward facilitation (FFF) and is due to differences in E/I ratios in different cortical layers (Adesnik and Scanziani, 2010). Given the abovementioned effects of LTPi-FFI on the E/I ratio and gain modulation of L5 PN output spiking, we hypothesized that L2/3-induced facilitation of deep cortical layer PNs could be affected by potentiation of local perisomatic inhibitory transmission. FFF can be induced in cortical slices by depolarizing ChR2+ L2/3 PNs with a 1-s-long ramp of blue light while simultaneously depolarizing L5 PNs (Adesnik and Scanziani, 2010). L5 PNs were depolarized with 1-s-long current injections to trigger AP firing (average rate, 5.4 ± 0.29 Hz, range, 2–8 Hz; n = 23; Figures 3A and 3C, baseline [Bsl], black trace, and gray bar), which was significantly increased by simultaneous photostimulation of L2/3 (average rate, 8.26 ± 0.35 Hz; range, 5–12 Hz; n = 23, Figures 3A and 3C, blue trace and bar, Bsl_light; $F(3,66) = 35.83$, $p < 0.0001$; $p < 0.0001$ for Bsl versus Bsl_light, Friedman test followed by Dunn's multiple comparison test). LTPi-FFI did not change the Bsl spike rate of L5 PNs (average rate, 5.873 ± 0.35 Hz; range, 3–8 Hz; n = 23; Figures 3B and 3C, black trace and dotted bar, LTPi), ruling out the possibility that postsynaptic burst firing alone altered L5 PN excitability. Remarkably, when the same experiment was repeated after inducing LTPi-FFI, facilitation of L5 PN excitability, triggered by L2/3 activation, was largely decreased (average rate, 6.22 ± 0.41 Hz; range, 2–10 Hz; n = 23; Figures 3B and 3C, red trace and red bar, LTPi_light; $F(3,66) = 35.83$, $p < 0.0001$; $p = 0.7218$ for LTPi versus LTPi_light, Friedman test followed by Dunn's multiple comparisons test).

Altogether, these results indicate that the cell-autonomous long-term strengthening of perisomatic inhibition can reduce or completely abolish coordination of cortical activity across cortical layers (Figure 3D).

LTPi-FFI Induces a Shift in Temporal Association of L5 PN Firing during Photo-Induced Rhythmic Activity

Perisomatic inhibition, particularly from PV basket cells, drives large populations of PNs, entraining them to network oscillations in the β-γ-frequency range (Buzsáki and Wang, 2012; Cardin et al., 2009; Sohal et al., 2009). Therefore, we hypothesized that changes in perisomatic inhibitory strength might affect the

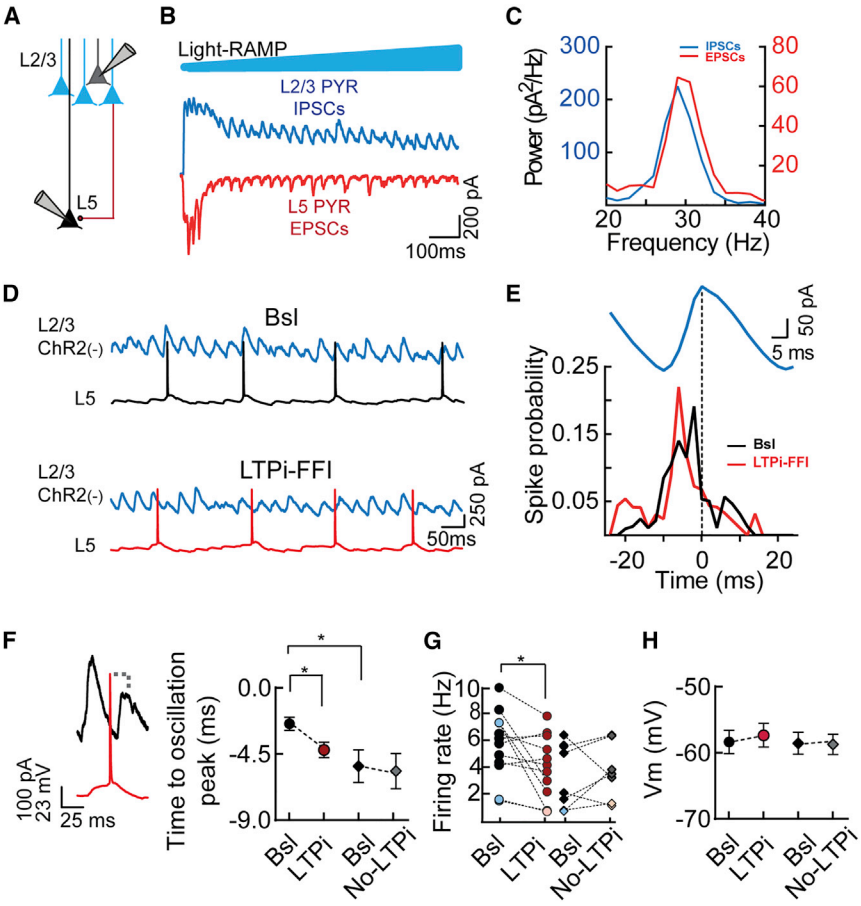

Figure 4. LTPi-FFI Induces a Shift in Temporal Association of L5 PN Firing during Photo-Induced Rhythmic Activity

(A) Scheme of the recording configuration.

(B) Representative traces during a light ramp (blue, 1-s duration) protocol inducing rhythmic activity of L2/3 IPSCs (blue trace) and L5 EPSCs (red trace).

(C) Power spectra of the EPSCs and IPSCs of the cells shown in (B).

(D) Representative firing activity of a L5 PN during γ-activity in L2/3 before (Bsl, black trace) and after induction of LTPi-FFI (red trace).

(E) Spike probability during a cycle (blue trace) of the same L5 PN before (black) and after LTPi-FFI (red).

(F) Left: representative traces illustrating the association of a spike of a L5 PN (red trace) with the peak of oscillating IPSCs from a L2/3 PN (black trace). Right: population data of the time to oscillation peak in cells that underwent LTPI-FFI (circles) and cells in which the postsynaptic bursts had no effect (diamonds). *$p < 0.05$, Wilcoxon matched-pairs signed-rank test (Bsl versus LTPi) and *$p < 0.05$, Kruskal-Wallis test followed by Dunn's multiple comparisons test (Bsl versus Bsl).

(G) Firing rates of LTPI-FFI (circles) and no LTPi cells (diamonds). Black and red dots (left), and black and gray diamonds (right) refer to PNs used for temporal association analysis. Cells indicated with blue and/or pink symbols had to be removed from the temporal association analysis because of spike sparsity. *$p < 0.05$, paired t test (Bsl versus LTPi).

(H) Average population data of the membrane resting potentials of LTPI-FFI (circles) and no LTPi cells (diamonds).

Population data are illustrated as mean ± SEM.

temporal association of PN firing with ongoing γ-activity. A well-characterized protocol to induce γ-oscillations in cortical slices is optogenetic stimulation with ramps of blue light, resulting in prolonged firing of ChR2-expressing L2/3 PNs (Adesnik and Scanziani, 2010; Deleuze et al., 2019). This protocol evoked robust γ-oscillations that depend on both GABAergic and glutamatergic synaptic transmission (Adesnik and Scanziani, 2010; Pouille et al., 2009; Shao et al., 2013). Importantly, photo-induced γ-activity is faithfully transmitted vertically to L5 PNs and PV cells belonging to the same cortical column (Adesnik and Scanziani, 2010; Pluta et al., 2019; Deleuze et al., 2019).

We induced oscillatory activity by photostimulation of ChR2+ L2/3 PNs while simultaneously recording inhibitory postsynaptic currents (IPSCs) and excitatory postsynaptic currents (EPSCs) in voltage clamp in ChR2-negative PNs in L2/3 and L5, respectively (average amplitude of IPSCs, 703.9 ± 82.45 pA; average amplitude of EPSCs, 266.8 ± 56.87 pA; n = 15; Figures 4A and 4B). Photostimulation induced robust oscillations in the γ-frequency range, involving both IPSCs and EPSCs, in L2/3 and L5 PNs, respectively (frequency IPSCs, 26.04 ± 0.78 Hz; frequency EPSCs, 27.26 ± 1.37 Hz; n = 15, p = 0.45, Wilcoxon matched-pairs signed-rank test; Figure 4C). We then recorded L5 PNs in current-clamp mode to analyze how their spikes were temporally associated with ongoing IPSC rhythmic activity, recorded in voltage-clamp in L2/3 PNS (Figures 4D and 4E). During baseline (Bsl), L5 PNs were tuned to γ-oscillations and discharged, on average, ~2 ms before the peak of the γ-cycle (spike time to oscillation peak during Bsl, −2.44 ± 0.44 ms, n = 9; Figures 4E and 4F). Remarkably, after inducing LTPi-FFI with bursts of APs, L5 PN firing was significantly anticipated (spike time to oscillations after AP bursts, −4.22 ± 0.52 ms, n = 9, p = 0.0313, Wilcoxon matched-pairs signed-rank test; Figures 4E and 4F). We restricted our analysis to a pool of PNs exhibiting sufficient spiking activity (>1 Hz) following LTPi. In these cells, the observed change in spike timing was not accompanied by changes in firing rate or resting membrane potential (Figures 4G and 4H, firing rate: 6.3 ± 0.61 Hz versus 4.8 ± 0.58 Hz, Bsl versus LTPi, respectively; paired t test, p = 0.0804; membrane potential: p = 0.49 for Bsl versus LTPi, paired t test). Importantly, however, when the firing frequency was analyzed for all PNs exhibiting LTPi, the firing frequency was significantly reduced in response to LTPi-inducing bursts (5.643 ± 0.7 versus 3.88 ± 0.67 Hz, Bsl versus LTPi, respectively; p = 0.0266, paired t test; Figure 4G). Interestingly, in cells in which LTPi-FFI could not be induced, we did not observe a change in timing association (Bsl time to oscillation peak, −5.33 ± 1.12 ms; after bursts, −5.67 ± 1.2 ms, n = 6; p = 0.36, paired t test; Figure 4F). Intriguingly, we found that PNs that did not express LTPi displayed a significantly longer time to oscillation peak (p = 0.0269, Kruskal-Wallis test followed by Dunn's multiple comparisons test), which was similar to that of PNs exhibiting plasticity (p = 1.0).

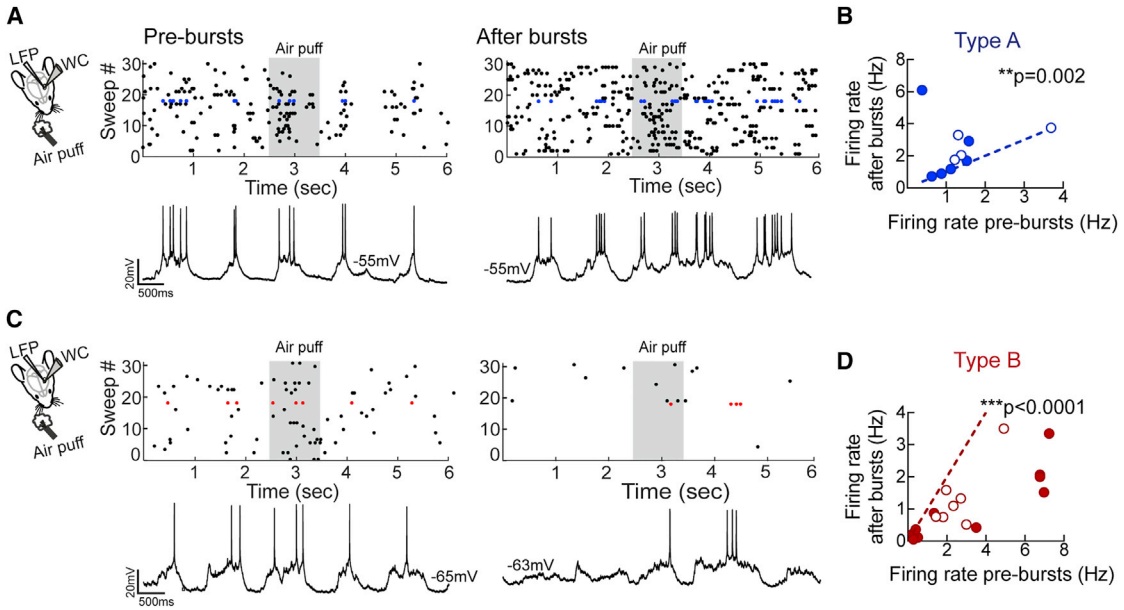

Figure 5. Bursts of APs Decrease the Firing Rate in a Subset of L5 PNs *In Vivo*

(A) Left: scheme of the recording configuration. Right: representative experiment of a type A PN (top, raster plot; bottom, representative current-clamp trace). Air puff stimulation is indicated as a gray rectangle during a pre- and post-burst period.

(B) Plot of the mean firing rate from individual PNs before (x axis) versus 5–10 min after postsynaptic bursts (y axis). Type A L5 PNs displayed a small but significant increase in firing rate after bursts. A dotted line indicates unitary values (no change). Blue-filled symbols refer to PNs receiving air puff stimulation; open circles refer to PNs, which did not receive air puff stimulation. Note that these are different cells from different recordings. **$p < 0.01$, Wilcoxon matched-pairs signed-rank test.

(C and D) The same as in (A) and (B) but for type B cells (C and D, respectively), in which postsynaptic bursts induced a decrease in firing rate under both conditions. ***$p < 0.0001$, Wilcoxon matched-pairs signed-rank test.

Population data are illustrated as mean ± SEM.

These results indicate that potentiation of feedforward perisomatic inhibition alters the temporal association of L5 PNs during γ-oscillations.

Bursts of APs Decrease the Firing Rate in a Subset of L5 PNs *In Vivo*

Do LTPi-inducing bursts also decrease L5 PN spikes *in vivo*? We performed whole-cell recordings from L5 PNs in the barrel cortex of anesthetized mice (STAR Methods) during spontaneous activity and in the presence of sensory stimulation induced by air puffs to the contralateral whisker pads. Location and PN identity were confirmed by anatomy in some experiments. Notably, 100% of recordings were in L5, as confirmed by labeling L4 in scnn1a-cre crossed with a td-Tomato reporter line (Figure S3). PNs could be separated into two populations according to their change in firing rate following AP bursts (5 APs at 100 Hz, repeated 15 times every 10 s). Type A cells displayed an increased firing rate upon LTPi-inducing bursts during spontaneous activity and in the presence of sensory stimulation (1.37 ± 0.28 versus 2.43 ± 0.52 Hz, pre-bursts versus after bursts, respectively; n = 10, p = 0.002, Wilcoxon matched-pairs signed-rank test; Figures 5A and 5B; Figure S4). Conversely, type B cells exhibited a marked decrease in firing rate (2.4 ± 0.56 versus 1.04 ± 0.26 Hz, pre-bursts versus after bursts, respectively; n = 16, p < 0.0001, Wilcoxon matched-pairs signed-rank test; Figures 5C, 5D and 4). Importantly, these changes were not associated with significant variations in membrane potential (type A: −57.9 ± 2.8 versus −55.4 ± 2.9 mV, pre-bursts versus after bursts; n = 10, p = 0.08, Wilcoxon matched-pairs signed-rank test; type B: −58.09 ± 2.9 versus −56.31 ± 2.0 mV, pre-bursts versus after bursts; n = 16, p = 0.25, Wilcoxon matched-pairs signed-rank test). The depth of patched neurons *in vivo* also did not differ between type A and B neurons (666.7 ± 21.08 μm depth versus 714.4 ± 21.35 μm depth, type A versus type B, respectively; p = 0.2440, Mann-Whitney test). Moreover, the Bsl spike frequency of type A and B neurons was not significantly different (p = 0.3767, Kruskal-Wallis test followed by Dunn's multiple comparisons test). Type A and B accounted for 38.5% and 61.5% of recorded PNs.

These results indicate that, *in vivo*, a prominent fraction of PNs respond to repetitive AP burst firing with a decreased firing rate, possibly through potentiation of perisomatic inhibition, similarly to our slice results.

A Reduced Firing Rate Is Associated with Increased Tuning of PN Spiking Activity with γ-Oscillations *In Vivo*

We found that LTPi is associated with altered temporal association of PN firing to photo-induced γ-oscillations in acute cortical slices (Figure 4). Photo-activated γ-oscillations are a very helpful strategy to study network activity in slice. However, their activation is somewhat artificial, and optogenetic hyper-synchrony can

affect oscillation temporal dynamics. We therefore examined whether postsynaptic bursting activity changes the temporal association of L5 PN firing with naturally occurring rhythmic activity *in vivo*. Previous evidence indicates that cortical PNs are poorly coupled to spontaneous and sensory evoked γ-activity (Perrenoud et al., 2016). Could increases in perisomatic inhibition facilitate tuning of PN spiking with ongoing network oscillations? *In vivo* whole-cell recordings of L5 PNs were coupled to local field potential (LFP) recordings obtained with a separate electrode (Figure S5; STAR Methods). We analyzed the relationship of spike probability of L5 PNs to γ-activity embedded in the LFP before and after bursting, in the presence and absence of sensory stimulation. As reported previously in the visual cortex (Perrenoud et al., 2016), PN spiking activity was poorly tuned in the presence and absence of whisker stimulation (Figure 6; Figure S6). On average, spike distributions did not reveal a significant phase preference under both conditions (Figure 6; Figure S6). However, in 8 of 11 cells recorded during spontaneous activity (n = 10 mice) and in 11 of 15 cells recorded during air puff stimulation (n = 13 mice), we observed a slight but significant increase in spike tuning with γ-activity. This was indicated by nonrandom spike-phase distributions crossing the Monte Carlo simulation threshold (STAR Methods; Figure 6; Figure S6).

Interestingly, in sensory evoked conditions, although type A cells did not exhibit any significant change in maximum (max) spike probability (Figures 6A–6C), type B displayed a significant increase in max spike probability after bursts (Figures 6D–6F; type A: 0.11 ± 0.016 versus 0.092 ± 0.011, Bsl versus after bursts, n = 6, p = 0.22, Wilcoxon matched-pairs signed-rank test; type B: 0.084 ± 0.007 versus 0.113 ± 0.007, Bsl versus after bursts, n = 9, p = 0.0039, Wilcoxon matched-pairs signed-rank test). Accordingly, after AP bursts, the fraction of type B neurons tuned to γ-activity increased (5 of 9 versus 8 of 9, Bsl versus after bursts, respectively). This was also reflected by an increased delta pairwise phase consistency (PPC), which is a measure of phase locking, independent of spike rate (Perrenoud et al., 2016; Veit et al., 2017; Figure S6H).

These results indicate that type B L5 PNs increase their tuning to γ-oscillations both during spontaneous and sensory evoked activity. This suggests that potentiation of inhibitory transmission likely promotes orchestrated activity of single PNs *in vivo*.

A Computational Model Reveals Two Separate Effects of LTPI-FFI

Our *in vitro* and *in vivo* results (Figures 4 and 6) suggest that LTPi alters the temporal association of PN firing during γ-oscillations. This prompts the question whether this is due to the actual strength of PN perisomatic inhibition, which sets the actual E/I level. To address this question, we examined a computational model of the FFI circuit between L2/3 and L5 (Figure 7A). In this model, a L5 PN was represented by an integrate-and-fire neuron, which was driven by L2/3 oscillatory activity (30 Hz) through a composite postsynaptic current (PSC, Figure 7B). As determined experimentally in response to brief L2/3 optical stimulation (Figures 1A–1C) or synaptic recordings (Lefort et al., 2009), the composite PSC consisted of an early excitatory component, followed, after a short delay, by an inhibitory component corresponding to FFI (STAR Methods). The amplitude of the inhibitory component was systematically varied to investigate the effects of LTPi-FFI in the model. Additional inputs to the L5 PN were modeled as background noise.

L2/3 oscillatory inputs filtered through the composite PSC led to temporal modulation of the activity in the model L5 PN (Figure 7C). To determine the temporal relationship between L5 and L2/3 activity, we computed the histograms of temporal activity in L5 and extracted its phase and amplitude by fitting cosine functions (Figure 7C). The phase of the histogram quantifies the average timing of L5 activity with respect to L2/3 oscillations, whereas the amplitude of the modulation represents the precision of L5 spikes. A mathematical analysis of the circuit dynamics predicted that the phase and amplitude of L5 PN activity are determined by the phase and amplitude of the Fourier transform of the composite PSC, evaluated at the frequency of 30 Hz, which corresponds to L2/3 oscillatory inputs (Figure 7B; STAR Methods). A comparison with numerical simulations confirmed this prediction (Figures 7D and 7E).

The circuit model revealed that increasing the amplitude of the inhibitory component of the composite PSC led to two separate effects. The first effect is that increasing inhibition at moderate strengths shifts the average timing of L5 activity with respect to L2/3 oscillations but leaves the precision of the activity essentially unchanged. This timing shift is consistent with the experimental measurements reported in Figure 4 (note that, in Figure 4, the absolute timing was quantified with respect to L2/3 IPSCs, whereas in the model, the timing is quantified with respect to L2/3 average firing activity). This shift can be understood by considering the histograms of activity in Figure 7C. If the composite PSC is dominantly excitatory (Figure 7C, leftmost column), then a peak in L2/3 activity (Figure 7C, top row) is followed by a peak in the L5 activity histogram (Figure 7C, bottom row). If the compound PSC is dominantly inhibitory (Figure 7C, rightmost column), a peak in L2/3 activity (Figure 7C, top row) is instead followed by a trough in the L5 activity histogram (Figure 7C, bottom row). In between these two extremes, increasing inhibition progressively shifts the trough in L5 activity earlier with respect to the peak of L2/3 inputs (Figure 7C, bottom row, dashed lines show the peak of L2/3 inputs).

The model shows that the range of possible timing shift is limited because the phase shift saturates as inhibition is increased. Interestingly, however, large increases in inhibition lead to a second, separate effect in which the timing of L5 activity does not change anymore, but its precision increases with stronger inhibition, as shown previously (Lourenço et al., 2014). Accordingly, this effect is consistent with increased tuning *in vivo*, shown in Figure 6. The difference in the overall amplitude of tuning to γ-oscillations between slices and *in vivo* conditions could be ascribed to different background noise levels, typical of slices versus *in vivo* conditions (Figure S7). However, both phase shift and increased tuning were present over a very broad range of background noise level (Figure S7).

DISCUSSION

In this study, we provide evidence that bursting activity of L5 PNs can potentiate incoming FFI recruited by a descending excitatory pathway, which is one of the most prominent in the neocortex. This plasticity likely originated from PV basket cells,

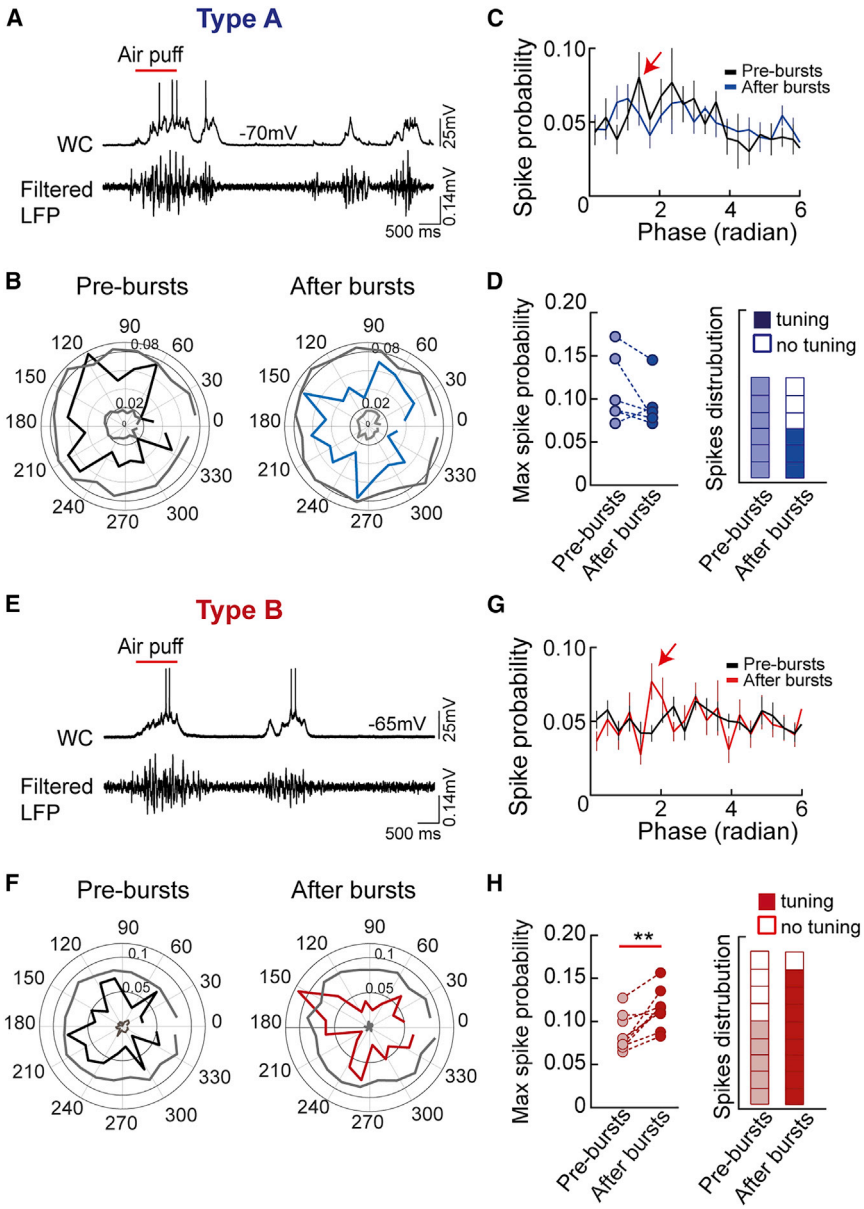

Figure 6. A Reduced Firing Rate Is Associated with Increased Tuning of PN Spiking Activity with γ-Oscillations *In Vivo*

(A) Top: current-clamp traces showing firing activity in a type A L5 PN (top trace) and filtered LFP (between 20 and 100 Hz, bottom trace). The red bar indicates air puff stimulation.

(B) Polar plots displaying the circular distribution of APs with γ-phases in the same type A neuron before (left, pre-bursts, black trace) and after bursts (right, post-bursts, blue trace). Gray lines refer to confidence intervals.

(C) Population spike distribution across the phase before (black trace) and after bursts (blue trace). Note the point of maximum (max) spike probability (red arrow).

(D) Summary plot of max spike probability extracted from each cell before (light blue circles) and after bursts (dark blue circles).

(E–H) The same as in (A)–(D) but for type B cells (E, F, G, and H, respectively). In these PNs, postsynaptic bursts induced a marked increase in max spike probability. **$p < 0.01$, Wilcoxon matched-pairs signed-rank test.

Population data are illustrated as mean ± SEM.

strongly modulated PN gain, affected coordinated activity across cortical layers, and altered the temporal association of PNs with γ-oscillations both *in vitro* and *in vivo*.

In principle, FFI can result from long-range recruitment of different interneuron subclasses (Pluta et al., 2019). However, potentiation of FFI likely involves perisomatic inhibition originating almost exclusively from PV basket cells. Indeed, here we provide evidence that optogenetic activation of L2/3 PNs efficiently recruits L5 PV basket cells (Figure S2). Moreover, LTPi-FFI was completely abolished by the canonical NO receptor inhibitor ODQ, which we previously showed to be selective for PV cell-mediated LTPi, and did not involve dendrite-targeting SST interneurons (Lourenço et al., 2014). Moreover, SST interneurons are recruited more efficiently in response to prolonged trains because of strongly facilitating glutamatergic synapses (Kapfer et al., 2007; Silberberg and Markram, 2007; Wang et al., 2004). Although we cannot exclude that other interneuron types might be involved in LTPi-FFI, we believe that this plasticity relies on the strength of PV cell synapses. Accordingly, PV basket cells have been demonstrated to be the most prominent, if not exclusive, providers of perisomatic inhibition onto large deep-layer PNs of the somatosensory cortex (Bodor et al., 2005) and to be the main source of evoked inhibition onto L5 PNs (Kruglikov and Rudy, 2008; Mateo et al., 2011).

Our data indicate that postsynaptic firing activity alone can effectively alter the E/I ratio of a prominent input pathway, impinging L5 PNs. A tight balance between excitation and inhibition is believed to guarantee proper functioning of neural circuits (Isaacson and Scanziani, 2011; Marín, 2012; Higley and Contreras, 2006; Okun and Lampl, 2008; Froemke et al., 2007; Wehr and Zador, 2003; Ferster, 1986; Hensch and Fagiolini, 2005). However, loosening of the E/I lock is necessary for sensory processing and refinement of sensory maps (Froemke et al., 2007). Moreover, it has been shown that the E/I ratio is different across individual cortical principal cells, depending on the specific layer (Adesnik and Scanziani, 2010) and the intrinsic activity state of each PN (Xue et al., 2014), demonstrating that the tight lock of the E/I ratio can be disrupted by perturbing pyramidal cell activity. Therefore, plasticity of GABAergic perisomatic FFI can be a relevant mechanism to tune PN sensitivity to process sensory information within the cortical column.

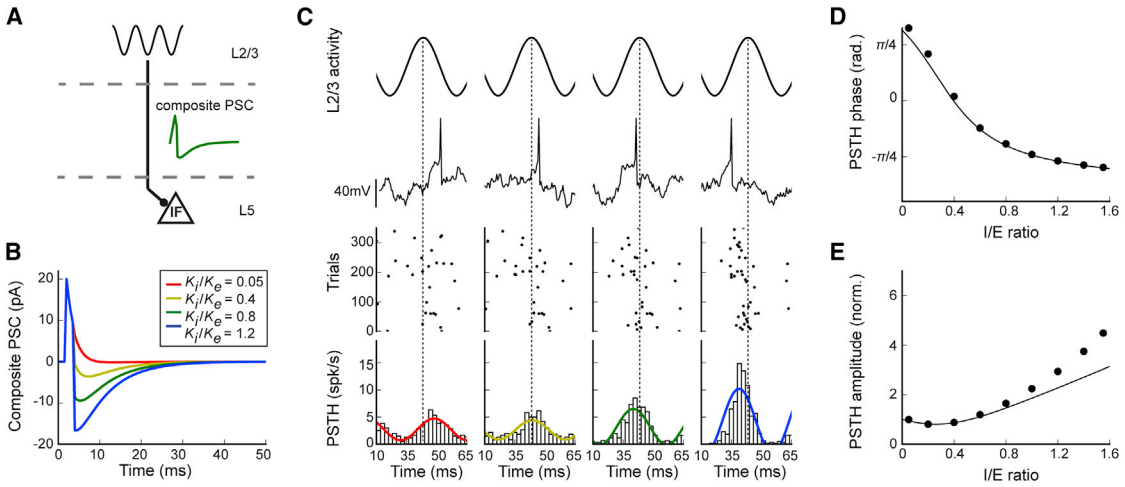

Figure 7. A Computational Model Reveals Two Separate Effects of LTPI-FFI

(A) Schematic of the model.

(B) Composite postsynaptic current received by the model L5 PN in response to a brief L2/3 activation for four increasing values of inhibitory strength.

(C) Activity in the model L5 PN in response to oscillatory L2/3 inputs for four increasing values of inhibitory strength (left to right). From top to bottom: L2/3 oscillation, membrane potential traces in the model L5 PN, rastergram of model L5 PN APs over 300 repeats of the input, and histogram of the average activity computed over 3,000 repeats of the input.

(D and E) Phase and amplitude of the average L5PN activity as function of the I/E ratio. Dots, results of cosine fits to simulation data (illustrated in the bottom panels in C); continuous line, theoretical prediction based on the shape of the composite PSC (STAR Methods). In (D), the phase is determined with respect to L2/3 input. In (E), the amplitude was normalized to 1 for an I/E ratio of 0.05. The theoretical prediction is based on a linear approximation. This approximation fails at large values of inhibition, as seen in the deviations between predicted and measured amplitude (E). Non-linear effects lead to an increase in peri-oscillation time histogram (POTH) amplitude and, therefore, firing precision, with respect to the linear prediction.

LTPi-FFI results in a strong divisive output modulation of the I/O curve because it significantly changed its slope without altering the rheobase. From a computational perspective, this means that, for rate-coded neuronal signaling, the modulation operated by LTPi-FFI results in a change of PN gain that affects the dynamic range of its response, likely preventing saturation of firing (Silver, 2010). However, whether inhibition plays an additive or multiplicative role has been debated, depending on the location (perisomatic versus dendritic) and strength of the inhibitory response as well as on the morphological complexity of the postsynaptic neuron (Lovett-Barron et al., 2012; Silver, 2010). In particular, perisomatic PV cell-mediated modulation of orientation tuning of visual cortical PNs has been shown to have both an additive and multiplicative effect with strong modulation of PN gain during sensory processing (Atallah et al., 2012; Lee et al., 2012; Wilson et al., 2012). Here we show that cell-autonomous potentiation of perisomatic inhibition has a strong effect on PN gain. This was not due to changes in intrinsic excitability (e.g., changes in membrane potential or resistance) but due to a selective increase in FFI. Therefore, by inducing retrograde potentiation of perisomatic inhibition, burst firing of PNs altered their functional network connectivity and, thus, the dynamic pattern of their activation through divisive modulation of their gain.

Cortical PNs are known to respond to sensory stimuli using a sparse population coding (Petersen and Crochet, 2013). In this regime, neurons act as coincidence detectors of temporally correlated input; changes in the gain of the I/O curve of PNs might shape the time window in which inputs can be integrated to generate a spike (Lourenço et al., 2014; Pouille and Scanziani, 2001). It is therefore likely that burst firing-induced potentiation of inhibition controls the temporal properties of signals propagating through the network.

The dynamic modulation of PN firing, induced by plasticity of FFI had a powerful effect on columnar integration of activity across cortical layers. Indeed, activation of L2/3 PNs has been shown to increase the firing of PNs in L5 of the same column (Adesnik and Scanziani, 2010; but see Pluta et al., 2019). LTP of FFI strongly diminished (in fact, on average, it abolished) L2/3-dependent activation of L5 PNs, affecting the flow of neuronal communication across cortical layers.

Here we show that induction of long-term plasticity of feedforward perisomatic inhibition shifted the temporal association of L5 PN spikes with photo-induced γ-oscillations. This effect was due to increased inhibition because glutamatergic neurotransmission and passive properties were not altered by postsynaptic burst firing.

Photo-activated γ-oscillations are a very useful tool to dissect the cellular and synaptic mechanisms underlying network synchronization (Adesnik and Scanziani, 2010; Quiquempoix et al., 2018). However, this approach suffers from some limitations; namely, hyper-synchronous activity induced by simultaneous prolonged activation of a large number of neurons in a reduced preparation. We therefore investigated whether LTPi-inducing trains could affect spike timing relative to endogenous γ-activity in a more intact preparation. We found that our *in vitro* and *in vivo* results converged: burst firing induced a decrease in firing rate in a prominent fraction of L5 PNs and improved tuning during

spontaneous and sensory evoked γ-activity. The modulation of spike association to network oscillations both *in vitro* and *in vivo* we show here is in line with the known function of perisomatic inhibition (particularly from PV basket cells) to entrain PNs during γ-activity (Bartos et al., 2007; Wang, 2010; Buzsáki and Silva, 2012; Cardin et al., 2009; Isaacson and Scanziani, 2011; Sohal et al., 2009; but see Veit et al., 2017).

Moreover, both *in vitro* and *in vivo* we found a similar low percentage of neurons that did not display LTPi and did not exhibit decreased firing rates, respectively. We termed these neurons type A in our *in vivo* recordings, and we speculate that they correspond to the fraction of PNs not expressing LTPi *in vitro*. In these PNs, coupling with network activity was not affected by burst firing. It is currently unclear whether these PNs belong to different cell types. Indeed, it has been demonstrated that thick-tufted, large, cortico-fugal PNs of the prefrontal cortex are preferentially innervated by PV cells compared with more slender, thin-tufted, cortico-cortical PNs (Allene et al., 2015; Lee et al., 2014). Alternatively, in this minority of PNs, the lack of LTPi expression could be due to already potentiated (and, hence, saturated) inhibition. This could explain the consistent negative shift of their spike times *in vitro* compared with PNs that did undergo LTPi. Moreover, bi-directional, activity-dependent changes in firing were reported in L5 PNs of the rat neocortex (Mahon and Charpier, 2012). Future experiments will be necessary to unequivocally determine the detailed morpho-functional properties of the small percentage of PNs lacking expression of GABAergic plasticity.

Importantly, our computational model revealed that increasing inhibition in the feedforward circuit induced two separate effects for different levels of the E/I ratio. If excitation dominates, then increasing inhibition modulates the timing of L5 spikes but not their precision with respect to L2/3 oscillations. This is indeed what we found during photo-activated γ-oscillations in neocortical slices. If, however, inhibition becomes stronger than excitation, then further increases in inhibition improve the precision of L5 spikes (as found in Lourenço et al., 2014) but do not additionally affect their timing. This could explain the improvement in tuning we detect *in vivo*, where assessing the actual E/I ratio is technically challenging and prone to strong biases. Modifying inhibition strength within different ranges may therefore lead to different functional consequences. The strength of inhibitory connections is known to control coherence in recurrent networks (Bartos et al., 2002; Brunel and Hakim, 1999; Brunel and Wang, 2003). Here, in contrast, we demonstrated its specific role in temporal organization of activity in FFI circuits independent of background noise level.

Therefore, plasticity of feedforward perisomatic inhibition by governing spike-time association of single PNs with ongoing γ-activity might be responsible for shifting their participation to distinct cell assemblies, reconfiguring the local network (Mongillo et al., 2018).

In conclusion, LTPi of feedforward inhibition can be a simple mechanism modulating the functional connectivity of single PNs, largely influencing cortical networks and subnetworks. LTPi of PV cell-mediated FFI in sensory cortices could be a fundamental dynamic property of cortical networks, providing the basis of diverse cognitive functions such as sensory perception and attention.

STAR★METHODS

Detailed methods are provided in the online version of this paper and include the following:

- KEY RESOURCES TABLE
- LEAD CONTACT AND MATERIALS AVAILABILITY
- EXPERIMENTAL MODEL AND SUBJECT DETAILS
- METHOD DETAILS
  - In utero electroporation
  - *In Vitro* Slice Preparation and Electrophysiology
  - *In vitro* data analysis
  - Photostimulation
  - Immunofluorescence
  - Preparation for *in vivo* electrophysiology
  - *In Vivo* LFP and whole-cell patch recording
  - Biocytin filling
  - Analysis of the phase modulation of AP-LFP coupling
  - Computational model
- QUANTIFICATION AND STATISTICAL ANALYSIS
- DATA AND CODE AVAILABILITY

SUPPLEMENTAL INFORMATION

Supplemental Information can be found online at https://doi.org/10.1016/j.celrep.2019.12.052.

ACKNOWLEDGMENTS

We thank Caroline Mailhes and Geeske M. van Woerden for initial help with *in utero* electroporation. We thank Michael Graupner and Christoph Schmidt-Hieber for advice regarding establishing the *in vivo* whole-cell recording technique. This work was supported by the European Research Council (ERC) under the European Community 7th Framework Program (FP7/2007-2013/ERC grant agreement 200808), "Investissements d'avenir" ANR-10-IAIHU-06, Agence Nationale de la Recherche (ANR-13-BSV4-0015-01, ANR-16-CE16-0007-02, ANR-17-CE16-0026-01, and ANR-18-CE16-0001-01), Fondation Recherche Médicale (Equipe FRM DEQ20150331684), a NARSAD independent investigator grant, and a grant from the Institut du Cerveau et de la Moelle Épinière (Paris) (to A.B.). S.O. was supported by the program Emergences of the City of Paris and the program "Investissements d'Avenir" launched by the French government and implemented by the ANR, with references ANR-10-LABX-0087 IEC and ANR- 11-IDEX-0001-02 PSL Research University.

AUTHOR CONTRIBUTIONS

Conceptualization, J.L. and A.B.; Methodology, J.L., A.M.D.S., A.P., C.D., A.A., M.G., M.B., and S.O.; Investigation, J.L., A.M.D.S., and M.B.; Formal Analysis, J.L., A.P., A.M.D.S., M.B., S.O., M.G., and A.B.; Writing – Original Draft, J.L. and A.B.; Writing – Review & Editing, J.L., S.O., and A.B.; Resources, S.O. and A.B.; Visualization, J.L., S.O., and A.B.; Supervision, J.L., S.O., and A.B.; Project Administration, J.L. and A.B.; Funding Acquisition, S.O. and A.B.

DECLARATION OF INTERESTS

The authors declare no competing interests.

Received: May 21, 2019
Revised: November 21, 2019
Accepted: December 13, 2019
Published: January 21, 2020

REFERENCES

Adesnik, H., and Scanziani, M. (2010). Lateral competition for cortical space by layer-specific horizontal circuits. Nature *464*, 1155–1160.

Allene, C., Lourenço, J., and Bacci, A. (2015). The neuronal identity bias behind neocortical GABAergic plasticity. Trends Neurosci. *38*, 524–534.

Ascoli, G.A., Alonso-Nanclares, L., Anderson, S.A., Barrionuevo, G., Benavides-Piccione, R., Burkhalter, A., Buzsáki, G., Cauli, B., Defelipe, J., Fairén, A., et al.; Petilla Interneuron Nomenclature Group (2008). Petilla terminology: nomenclature of features of GABAergic interneurons of the cerebral cortex. Nat. Rev. Neurosci. *9*, 557–568.

Atallah, B.V., and Scanziani, M. (2009). Instantaneous modulation of gamma oscillation frequency by balancing excitation with inhibition. Neuron *62*, 566–577.

Atallah, B.V., Bruns, W., Carandini, M., and Scanziani, M. (2012). Parvalbumin-expressing interneurons linearly transform cortical responses to visual stimuli. Neuron *73*, 159–170.

Bartos, M., Vida, I., Frotscher, M., Meyer, A., Monyer, H., Geiger, J.R., and Jonas, P. (2002). Fast synaptic inhibition promotes synchronized gamma oscillations in hippocampal interneuron networks. Proc. Natl. Acad. Sci. USA *99*, 13222–13227.

Bartos, M., Vida, I., and Jonas, P. (2007). Synaptic mechanisms of synchronized gamma oscillations in inhibitory interneuron networks. Nat. Rev. Neurosci. *8*, 45–56.

Bodor, A.L., Katona, I., Nyíri, G., Mackie, K., Ledent, C., Hájos, N., and Freund, T.F. (2005). Endocannabinoid signaling in rat somatosensory cortex: laminar differences and involvement of specific interneuron types. J. Neurosci. *25*, 6845–6856.

Brunel, N., and Hakim, V. (1999). Fast global oscillations in networks of integrate-and-fire neurons with low firing rates. Neural Comput. *11*, 1621–1671.

Brunel, N., and Hakim, V. (2008). Sparsely synchronized neuronal oscillations. Chaos *18*, 015113.

Brunel, N., and Wang, X.J. (2003). What determines the frequency of fast network oscillations with irregular neural discharges? I. Synaptic dynamics and excitation-inhibition balance. J. Neurophysiol. *90*, 415–430.

Brunel, N., Chance, F.S., Fourcaud, N., and Abbott, L.F. (2001). Effects of synaptic noise and filtering on the frequency response of spiking neurons. Phys. Rev. Lett. *86*, 2186–2189.

Buzsáki, G. (2010). Neural syntax: cell assemblies, synapsembles, and readers. Neuron *68*, 362–385.

Buzsáki, G., and Silva, F.L. (2012). High frequency oscillations in the intact brain. Prog. Neurobiol. *98*, 241–249.

Buzsáki, G., and Wang, X.J. (2012). Mechanisms of gamma oscillations. Annu. Rev. Neurosci. *35*, 203–225.

Carandini, M., and Heeger, D.J. (2011). Normalization as a canonical neural computation. Nat. Rev. Neurosci. *13*, 51–62.

Cardin, J.A., Carlén, M., Meletis, K., Knoblich, U., Zhang, F., Deisseroth, K., Tsai, L.H., and Moore, C.I. (2009). Driving fast-spiking cells induces gamma rhythm and controls sensory responses. Nature *459*, 663–667.

Castillo, P.E., Chiu, C.Q., and Carroll, R.C. (2011). Long-term plasticity at inhibitory synapses. Curr. Opin. Neurobiol. *21*, 328–338.

Chiu, C.Q., Martenson, J.S., Yamazaki, M., Natsume, R., Sakimura, K., Tomita, S., Tavalin, S.J., and Higley, M.J. (2018). Input-Specific NMDAR-Dependent Potentiation of Dendritic GABAergic Inhibition. Neuron *97*, 368–377.e3.

Chiu, C.Q., Barberis, A., and Higley, M.J. (2019). Preserving the balance: diverse forms of long-term GABAergic synaptic plasticity. Nat. Rev. Neurosci. *20*, 272–281.

Deleuze, C., Bhumbra, G.S., Pazienti, A., Lourenço, J., Mailhes, C., Aguirre, A., Beato, M., and Bacci, A. (2019). Strong preference for autaptic self-connectivity of neocortical PV interneurons facilitates their tuning to γ-oscillations. PLoS Biol. *17*, e3000419.

Douglas, R., Markram, H., and Martin, K. (2004). Neocortex. In The Synaptic Organization of the Brain, G. Shepherd, ed. (Oxford University Press), pp. 499–558.

Feldmeyer, D. (2012). Excitatory neuronal connectivity in the barrel cortex. Front. Neuroanat. *6*, 24.

Ferster, D. (1986). Orientation selectivity of synaptic potentials in neurons of cat primary visual cortex. J. Neurosci. *6*, 1284–1301.

Fourcaud-Trocmé, N., Hansel, D., van Vreeswijk, C., and Brunel, N. (2003). How spike generation mechanisms determine the neuronal response to fluctuating inputs. J. Neurosci. *23*, 11628–11640.

Freund, T.F., and Katona, I. (2007). Perisomatic inhibition. Neuron *56*, 33–42.

Froemke, R.C., Merzenich, M.M., and Schreiner, C.E. (2007). A synaptic memory trace for cortical receptive field plasticity. Nature *450*, 425–429.

Garkun, Y., and Maffei, A. (2014). Cannabinoid-dependent potentiation of inhibition at eye opening in mouse V1. Front. Cell. Neurosci. *8*, 46.

Griffen, T.C., and Maffei, A. (2014). GABAergic synapses: their plasticity and role in sensory cortex. Front. Cell. Neurosci. *8*, 91.

Gunaydin, L.A., Yizhar, O., Berndt, A., Sohal, V.S., Deisseroth, K., and Hegemann, P. (2010). Ultrafast optogenetic control. Nat. Neurosci. *13*, 387–392.

Hensch, T.K., and Fagiolini, M. (2005). Excitatory-inhibitory balance and critical period plasticity in developing visual cortex. Prog. Brain Res. *147*, 115–124.

Higley, M.J., and Contreras, D. (2006). Balanced excitation and inhibition determine spike timing during frequency adaptation. J. Neurosci. *26*, 448–457.

Isaacson, J.S., and Scanziani, M. (2011). How inhibition shapes cortical activity. Neuron *72*, 231–243.

Jiang, X., Shen, S., Cadwell, C.R., Berens, P., Sinz, F., Ecker, A.S., Patel, S., and Tolias, A.S. (2015). Principles of connectivity among morphologically defined cell types in adult neocortex. Science *350*, aac9462.

Kapfer, C., Glickfeld, L.L., Atallah, B.V., and Scanziani, M. (2007). Supralinear increase of recurrent inhibition during sparse activity in the somatosensory cortex. Nat. Neurosci. *10*, 743–753.

Kepecs, A., and Fishell, G. (2014). Interneuron cell types are fit to function. Nature *505*, 318–326.

Kruglikov, I., and Rudy, B. (2008). Perisomatic GABA release and thalamocortical integration onto neocortical excitatory cells are regulated by neuromodulators. Neuron *58*, 911–924.

Kurotani, T., Yamada, K., Yoshimura, Y., Crair, M.C., and Komatsu, Y. (2008). State-dependent bidirectional modification of somatic inhibition in neocortical pyramidal cells. Neuron *57*, 905–916.

Lee, S.H., Kwan, A.C., Zhang, S., Phoumthipphavong, V., Flannery, J.G., Masmanidis, S.C., Taniguchi, H., Huang, Z.J., Zhang, F., Boyden, E.S., et al. (2012). Activation of specific interneurons improves V1 feature selectivity and visual perception. Nature *488*, 379–383.

Lee, A.T., Gee, S.M., Vogt, D., Patel, T., Rubenstein, J.L., and Sohal, V.S. (2014). Pyramidal neurons in prefrontal cortex receive subtype-specific forms of excitation and inhibition. Neuron *81*, 61–68.

Lefort, S., Tomm, C., Floyd Sarria, J.C., and Petersen, C.C. (2009). The excitatory neuronal network of the C2 barrel column in mouse primary somatosensory cortex. Neuron *61*, 301–316.

Lourenço, J., Pacioni, S., Rebola, N., van Woerden, G.M., Marinelli, S., DiGregorio, D., and Bacci, A. (2014). Non-associative potentiation of perisomatic inhibition alters the temporal coding of neocortical layer 5 pyramidal neurons. PLoS Biol. *12*, e1001903.

Lovett-Barron, M., Turi, G.F., Kaifosh, P., Lee, P.H., Bolze, F., Sun, X.H., Nicoud, J.F., Zemelman, B.V., Sternson, S.M., and Losonczy, A. (2012). Regulation of neuronal input transformations by tunable dendritic inhibition. Nat. Neurosci. *15*, 423–430, S1–S3.

Mahon, S., and Charpier, S. (2012). Bidirectional plasticity of intrinsic excitability controls sensory inputs efficiency in layer 5 barrel cortex neurons in vivo. J. Neurosci. *32*, 11377–11389.

Malenka, R.C. (2003). The long-term potential of LTP. Nat. Rev. Neurosci. *4*, 923–926.

Manent, J.B., Wang, Y., Chang, Y., Paramasivam, M., and LoTurco, J.J. (2009). Dcx reexpression reduces subcortical band heterotopia and seizure threshold in an animal model of neuronal migration disorder. Nat. Med. *15*, 84–90.

Manseau, F., Marinelli, S., Méndez, P., Schwaller, B., Prince, D.A., Huguenard, J.R., and Bacci, A. (2010). Desynchronization of neocortical networks by asynchronous release of GABA at autaptic and synaptic contacts from fast-spiking interneurons. PLoS Biol. *8*, e1000492.

Margrie, T.W., Brecht, M., and Sakmann, B. (2002). In vivo, low-resistance, whole-cell recordings from neurons in the anaesthetized and awake mammalian brain. Pflugers Arch. *444*, 491–498.

Marín, O. (2012). Interneuron dysfunction in psychiatric disorders. Nat. Rev. Neurosci. *13*, 107–120.

Mateo, C., Avermann, M., Gentet, L.J., Zhang, F., Deisseroth, K., and Petersen, C.C. (2011). In vivo optogenetic stimulation of neocortical excitatory neurons drives brain-state-dependent inhibition. Curr. Biol. *21*, 1593–1602.

Méndez, P., and Bacci, A. (2011). Assortment of GABAergic plasticity in the cortical interneuron melting pot. Neural Plast. *2011*, 976856.

Mongillo, G., Rumpel, S., and Loewenstein, Y. (2018). Inhibitory connectivity defines the realm of excitatory plasticity. Nat. Neurosci. *21*, 1463–1470.

Murphy, B.K., and Miller, K.D. (2003). Multiplicative gain changes are induced by excitation or inhibition alone. J. Neurosci. *23*, 10040–10051.

Okun, M., and Lampl, I. (2008). Instantaneous correlation of excitation and inhibition during ongoing and sensory-evoked activities. Nat. Neurosci. *11*, 535–537.

Perrenoud, Q., Pennartz, C.M., and Gentet, L.J. (2016). Membrane Potential Dynamics of Spontaneous and Visually Evoked Gamma Activity in V1 of Awake Mice. PLoS Biol. *14*, e1002383.

Petersen, C.C., and Crochet, S. (2013). Synaptic computation and sensory processing in neocortical layer 2/3. Neuron *78*, 28–48.

Petreanu, L., Huber, D., Sobczyk, A., and Svoboda, K. (2007). Channelrhodopsin-2-assisted circuit mapping of long-range callosal projections. Nat. Neurosci. *10*, 663–668.

Petrini, E.M., Ravasenga, T., Hausrat, T.J., Iurilli, G., Olcese, U., Racine, V., Sibarita, J.B., Jacob, T.C., Moss, S.J., Benfenati, F., et al. (2014). Synaptic recruitment of gephyrin regulates surface GABAA receptor dynamics for the expression of inhibitory LTP. Nat. Commun. *5*, 3921.

Pluta, S.R., Telian, G.I., Naka, A., and Adesnik, H. (2019). Superficial layers suppress the deep layers to fine-tune cortical coding. J. Neurosci. *39*, 2052–2064.

Pouille, F., and Scanziani, M. (2001). Enforcement of temporal fidelity in pyramidal cells by somatic feed-forward inhibition. Science *293*, 1159–1163.

Pouille, F., Marin-Burgin, A., Adesnik, H., Atallah, B.V., and Scanziani, M. (2009). Input normalization by global feedforward inhibition expands cortical dynamic range. Nat. Neurosci. *12*, 1577–1585.

Quiquempoix, M., Fayad, S.L., Boutourlinsky, K., Leresche, N., Lambert, R.C., and Bessaih, T. (2018). Layer 2/3 Pyramidal Neurons Control the Gain of Cortical Output. Cell Rep. *24*, 2799–2807.e4.

Rothman, J.S., Cathala, L., Steuber, V., and Silver, R.A. (2009). Synaptic depression enables neuronal gain control. Nature *457*, 1015–1018.

Sachdev, R.N., Krause, M.R., and Mazer, J.A. (2012). Surround suppression and sparse coding in visual and barrel cortices. Front. Neural Circuits *6*, 43.

Shao, Y.R., Isett, B.R., Miyashita, T., Chung, J., Pourzia, O., Gasperini, R.J., and Feldman, D.E. (2013). Plasticity of recurrent l2/3 inhibition and gamma oscillations by whisker experience. Neuron *80*, 210–222.

Silberberg, G., and Markram, H. (2007). Disynaptic inhibition between neocortical pyramidal cells mediated by Martinotti cells. Neuron *53*, 735–746.

Silver, R.A. (2010). Neuronal arithmetic. Nat. Rev. Neurosci. *11*, 474–489.

Sohal, V.S., Zhang, F., Yizhar, O., and Deisseroth, K. (2009). Parvalbumin neurons and gamma rhythms enhance cortical circuit performance. Nature *459*, 698–702.

Tremblay, R., Lee, S., and Rudy, B. (2016). GABAergic Interneurons in the Neocortex: From Cellular Properties to Circuits. Neuron *91*, 260–292.

Ulrich, D., and Huguenard, J.R. (1996). GABAB receptor-mediated responses in GABAergic projection neurones of rat nucleus reticularis thalami in vitro. J. Physiol. *493*, 845–854.

Veit, J., Hakim, R., Jadi, M.P., Sejnowski, T.J., and Adesnik, H. (2017). Cortical gamma band synchronization through somatostatin interneurons. Nat. Neurosci. *20*, 951–959.

Vickers, E.D., Clark, C., Osypenko, D., Fratzl, A., Kochubey, O., Bettler, B., and Schneggenburger, R. (2018). Parvalbumin-Interneuron Output Synapses Show Spike-Timing-Dependent Plasticity that Contributes to Auditory Map Remodeling. Neuron *99*, 720–735.e6.

Vogels, T.P., Sprekeler, H., Zenke, F., Clopath, C., and Gerstner, W. (2011). Inhibitory plasticity balances excitation and inhibition in sensory pathways and memory networks. Science *334*, 1569–1573.

Wang, X.J. (2010). Neurophysiological and computational principles of cortical rhythms in cognition. Physiol. Rev. *90*, 1195–1268.

Wang, Y., Toledo-Rodriguez, M., Gupta, A., Wu, C., Silberberg, G., Luo, J., and Markram, H. (2004). Anatomical, physiological and molecular properties of Martinotti cells in the somatosensory cortex of the juvenile rat. J. Physiol. *561*, 65–90.

Wehr, M., and Zador, A.M. (2003). Balanced inhibition underlies tuning and sharpens spike timing in auditory cortex. Nature *426*, 442–446.

Wilson, N.R., Runyan, C.A., Wang, F.L., and Sur, M. (2012). Division and subtraction by distinct cortical inhibitory networks in vivo. Nature *488*, 343–348.

Xue, M., Atallah, B.V., and Scanziani, M. (2014). Equalizing excitation-inhibition ratios across visual cortical neurons. Nature *511*, 596–600.

STAR★METHODS

KEY RESOURCES TABLE

REAGENT or RESOURCE	SOURCE	IDENTIFIER
Chemicals, Peptides, and Recombinant Proteins		
ODQ	R&D Systems Europe	0880
SR 95531 hydrobromide	R&D Systems Europe	15753
Biocytin	Sigma	B4261
Bupivacaine hydrochloride	Sigma	B1160000
Buprenorphine (Buprecare)	Centravet	BUP002
Atropine	ICM Animal House Pharmacy	N/A
Dexametosone (DEXAFORT)	Centravet	DEX211
Fast Green	Sigma	F7252
Critical Commercial Assays		
DAB substrate kit for peroxidase	VECTASTAIN Elite	SK-4100
ABC kit	VECTASTAIN Elite	PK-6100
Experimental Models: Organisms/Strains		
Mice: C57BL6/6J	Janvier	SC-C57J-F
Mice: Ai14	Jackson	RRID:IMSR_JAX:007914
Mice: Scnn1a-Tg3-Cre	Jackson	RRID:IMSR_JAX:009613
Mice: Swiss	Janvier	SN-SWISS-F
Recombinant DNA		
p-Lenti-CaMKIIa-ChETA-EYFP	Addgene	RRID:Addgene_26967
pCAG-mRFP	Addgene	RRID:Addgene_28311
pCAG-ChR2-Venus	Addgene	RRID:Addgene_15753
p-ChETA-EYFP	iVector (ICM)	Subcloned from p-Lenti-CaMKIIa-ChETA-EYFP
Software and Algorithms		
pClamp 10.3	Molecular Devices	https://www.moleculardevices.com/products/axon-patch-clamp-system/acquisition-and-analysis-software/pclamp-software-suite
IGOR PRO 5.0	Wavemetrics	https://www.wavemetrics.com/
Prism	Prism-GraphPad	https://www.graphpad.com/scientific-software/prism/
MATLAB	Mathworks	https://www.mathworks.com/
Detector – custom written software	J. R. Huguenard, Stanford UniversityJ. R. Huguenard, Stanford University	https://hlab.stanford.edu/wdetecta.php
Deposited Data		
Datasets	Mendeley Data	https://data.mendeley.com/datasets/75t97ncb24/2
Theoretical Model	GitHub	https://github.com/MathildeBigot

LEAD CONTACT AND MATERIALS AVAILABILITY

Further information and requests for resources and reagents should be directed to and will be fulfilled by the Lead Contact, Alberto Bacci (alberto.bacci@icm-institute.org). All unique reagents generated in this study are available from the Lead Contact without restriction.

EXPERIMENTAL MODEL AND SUBJECT DETAILS

Experimental procedures followed national and European (2010/63/EU) guidelines, and have been approved by the authors' institutional review boards and national authorities. All efforts were made to minimize suffering and reduce the number of animals.

Experiments were performed on 15- to 28-day-old C57BL/6 wild-type mice (Janvier Labs, France) or Scnn1a-Tg3-Cre mice expressing Cre recombinase under the control of the *Scnn1a* (sodium channel, nonvoltage-gated 1 alpha; Jackson) crossed with Ai9 mice, which have a *loxP*-flanked STOP cassette preventing transcription of a CAG promoter-driven red fluorescent protein variant (tdTomato) - all inserted into the *Gt(ROSA)26Sor* locus (Jackson). Mice used in this study were of both sexes.

METHOD DETAILS

In utero electroporation

Timed-pregnant C57BL/6 wild-type female mice (15.5 days postcoitum) were anaesthetized with 1%–2% isoflurane. The abdomen was cleaned with 70% ethanol and swabbed with betadine. Buprenorphine (0.05 mg/kg) was administered subcutaneously for preoperative analgesia and local anesthetic bupivacaine (2.5mg/kg) was injected between the skin and the abdomen 5 min before incision. A midline ventral laparotomy (~2 cm) was performed, and the uterus gently exposed and moistened with PBS, pre-warmed at 37°C. Using glass beveled capillaries, DNA plasmids mixed in saline (PBS) solution and 0.025% Fast Green (Sigma) were injected through the uterine wall into the lateral ventricle of each embryo. Embryos were injected with pCAG-mRFP (0.8 μg/μl) (Manent et al., 2009) (Addgene #28311) plasmid DNA mixed with either pCAG-ChR2-Venus (Petreanu et al., 2007) (Addgene #15753) or pCAG-ChETA-EYFP (1.5 μg/μL). ChETA-EYFP was subcloned from p-Lenti-CaMKIIa-ChETA-EYFP (Gunaydin et al., 2010) (Addgene #26967) into the backbone of pCAG-ChR2. After each injection, the embryos were moistened with PBS. DNA was electroporated via 5 square electrical pulses of 40 V amplitude and 50 ms duration through forceps-type circular electrodes positioned at 0° angle with respect to the rostral-caudal axis of the head of the embryos. After electroporation, the uterus was placed back into the peritoneal cavity and moistened with PBS. The abdomen and skin were then sutured and the latter cleaned with betadine. The procedure typically lasted maximum 40 min starting from anesthesia induction. Pups were born by natural birth and placed with a Swiss foster mother (timed-pregnant at the same time as C57BL/6 females) after they were screened for location and strength of transfection by trans-cranial epifluorescence under a fluorescence stereoscope.

In Vitro Slice Preparation and Electrophysiology

Coronal slices (400-μm-thick) from somatosensory cortex were obtained from 15- to 28-day-old C57BL/6 mice. Animals were deeply anesthetized with isofluorane and decapitated. Brains were quickly removed and immerse in ''cutting'' solution (4°C) containing the following (in mM): 87 NaCl, 25 $NaHCO_3$, 2.5 KCl, 1.25 NaH_2PO_4, 7.5 $MgSO_4$, 0.5 $CaCl_2$, 2 pyruvic acid, 3 myo-inositol, 0.4 ascorbic acid, 25 glucose and 70 sucrose (equilibrated with 95% O_2 / 5% CO_2). Slices were cut with a vibratome (Leica) in cutting solution and then incubated in oxygenated artificial cerebrospinal fluid (ASCF) containing the following (in mM): 125 NaCl, 3 KCl, 2.5 $CaCl_2$, 1.3 $MgSO_4$, 1.25 mM NaH_2PO_4, 26 mM $NaHCO_3$, 2 pyruvic acid, 3 myo-inositol, 0.4 ascorbic acid and 16 mM glucose (pH 7.4), initially at 34°C for 30 min, and subsequently at room temperature, before being transfer to the recording chamber. Recordings were obtained at 30°C. Synaptic events were recorded in whole-cell, voltage- or current-clamp mode from L2/3 and deep L5 PNs of mouse primary barrel somatosensory cortex visually identified using infrared video microscopy (Lourenço et al., 2014). For voltage clamp experiments of L2/3 PNs, electrodes (with a tip resistance of 2-4 MΩ) were filled with a cesium-based internal solution (in mM): 120 $CsMeSO_4$, 8 CsCl, 10 HEPES, 10 BAPTA, 4 NaCl, 2 $CaCl_2$, 4 Mg-ATP, 0.3 Na-GTP, 4 phosphocreatine di(tris), 0.5 QX-314-Cl; pH adjusted to 7.2 with CsOH; 280-300 mOsm. Under these recording conditions, activation of $GABA_A$ receptors resulted in outward currents at a holding potential (V_h) of +10 mV. In current clamp experiments electrodes were filled with a potassium-based intracellular solution containing (in mM): 130 K-gluconate, 3 KCl, 10 HEPES, 0.2 EGTA, 2 $MgCl_2$, 4 Mg-ATP, 0.3 Na-GTP, 4 phosphocreatine di(tris); pH adjusted to 7.2 with KOH; 280-300 mOsm. E_{Cl} was approximately −77 mV based on the Nernst equation, without correction for gluconate-generated liquid junction potential. In current-clamp mode cells were recorded at their resting membrane potential unless for Figure 4 where occasionally depolarization (max. current injection 30pA) was required in order to induce firing of L5 PN upon L2/3 light activation. In voltage-clamp experiments, access resistance was on average < 20 MΩ and monitored throughout the experiment. Recordings were discarded from analysis if the resistance changed by > 20% over the course of the experiment. In current-clamp experiments, input resistance was monitored with small current steps (−30 pA for 600 ms) and cells were excluded if it changed by > 25%. ODQ was obtain from R&D Systems Europe.

In vitro data analysis

Signals were amplified, using a Multiclamp 700B patch-clamp amplifier (Axon Instruments, Foster City, California, United States), sampled at 50 kHz and filtered at 4 or 10 kHz for voltage and current-clamp mode, respectively. Data were analyzed using pClamp (Axon Instruments), IGOR PRO 5.0, (Wavemetrics), MATLAB (MathWorks) and GraphPad Prism software.

IPSCs during rhythmic activity in vitro

Custom written software (Detector, courtesy J. R. Huguenard, Stanford University) was used for analyzing GABAergic events, as previously described (Manseau et al., 2010; Ulrich and Huguenard, 1996). Briefly, individual events were detected with a threshold-triggered process from a differentiated copy of the real trace. For each cell, the detection criteria (threshold and duration of trigger for detection) were adjusted to ignore slow membrane fluctuations and electric noise while allowing maximal discrimination of IPSCs. Detection frames were regularly inspected visually to ensure that the detector was working properly.

Spike probability of L5 PNs during rhythmic activity in vitro

Analysis of the temporal relationship between L5 PNs spikes and ongoing rhythmic activity was analyzed using custom written scripts in MATLAB (The MathWorks, Inc., Natick, Massachusetts, United States). Briefly, spikes were extracted using a threshold of −10 mV on the membrane potential trace, and the times of the action potential peaks were extracted after cubic spline data interpolation of the waveforms around the spikes. Next, IPSC peak positions from the detector (see above) were adjusted with a 50-samples smoothing of the current waveform, and delays between action potential timing and IPSC occurrence were computed. Finally, histograms between spike times and IPSC occurrences were generated using 2 ms binning and converted into probability distributions. Due to strong reduction of spike rates following LTPi induction, analysis of spike timing was restricted to PNs exhibiting a sufficient number of spikes after LTPi-inducing bursts.

Photostimulation

ChR2 or ChETA activation was induced by light flashes on cortical slices, using a 20 mW LED (λ = 470 nm, Cairn research, UK) collimated and coupled to the epifluorescence path of a Zeiss AxioExaminer microscope, using a 40X water immersion (N.A. 1) lens. In order to trigger robust oscillations (Figure 4), light ramps had a duration of 1–2 s, started at zero intensity and reached a final intensity of 9 mW/mm^2. The illuminated area was measured by bleaching coverslipped fluorescein. The light power was calculated with a power-meter at the tip of the 40X objective and was not corrected for the actual intensity at the tissue. The stimulus intensity was adapted to each slice, depending on the opsin expression and it was repeated with a frequency of 0.025 Hz. ChR2 activation was also obtained by brief square light pulses (ranging between 0.5 and 1 ms) evoking postsynaptic potentials in L5 PNs (Figure 1).

Immunofluorescence

In order to check proper electroporation of both plasmids in the somatosensory cortex, in some cases (Figure 1A), slices used for electrophysiology experiments were fixed overnight in 4% paraformaldehyde in phosphate buffer (PB, pH 7.4) at 4°C. Slices were then rinsed three times at room temperature (10 min each time) in PB and were then rinsed three times in PB (10 min each) at room temperature and coverslipped in mounting medium. Immunofluorescence was then observed with an ApoTome.2 microscope (Zeiss) and images were acquired using a 10x objective.

Preparation for *in vivo* electrophysiology

Two- to three-week-old naive C57BL/6 or Scnn1a x tdTomato mice of both sexes were anesthetized via intraperitoneal (i.p.) injection with 18% urethane (1.8 g/kg in sodium lactate ringer solution) and placed on a stereotaxic apparatus. The body temperature was constantly monitored and kept at 37°C with a heating blanket. Eye ointment was applied to prevent dehydration. To ensure a deep and constant level of anesthesia, vibrissae movement, eyelid reflex, response to tail, and toe pinching were visually controlled before and during the surgery. Subcutaneous injections of atropine (0.07 mg/kg) and dexamethasone (0.2 mg/kg) were used to maintain clear airways and prevent edema, respectively. A mix of local lidocaine and bupivacaine injection was performed over the cranial area of interest and, after a few minutes, a longitudinal incision was performed to expose the skull. A stainless steel head post was sealed on to the mouse skull using dental acrylic cement. A small craniotomy ($\geq$1 mm diameter) was made on the right hemisphere to target the primary somatosensory cortex according to stereotaxic coordinates at −1 from bregma: 3 lateral). A second small craniotomy (approximately 200 μm far from the previous) was drilled for the separate entry of the LFP pipette. Dura was not removed. The exposed cortical surface was superfused with warm HEPES-buffered extracellular solution (in mM: 125 NaCl, 5 KCl, 10 glucose, 10 HEPES, 1.8 CaCl2 and 1 MgSO4 (pH 7.2)) in order to maintain ionic balance and prevent desiccation.

In Vivo LFP and whole-cell patch recording

Patch pipettes (5-7 MΩ) of 1.5 mm external diameter borosilicate glass (WPI) were pulled on a Narishige P100 Vertica Puller and filled with (in mM): 135 K-gluconate, 6 KCl, 10 HEPES, 1 EGTA, 4 MgATP, Na2ATP and 8 phosphocreatin, pH adjusted to 7.2 with KOH, 290-295 mOsm. Pipette capacitance was neutralized before break-in. Whole-cell patch-clamp recordings of L5 pyramidal neurons were performed following the standard techniques for blind patching (Margrie et al., 2002). High positive pressure was applied to the pipette to prevent tip occlusion. After breaking the meninges, the positive pressure was immediately reduced to prevent cortical damage. Once reached L5 depth (~700 μm depth), the pipette was then advanced in 2-μm steps, and pipette resistance was monitored in the conventional voltage clamp configuration. When the pipette resistance suddenly increased, positive pressure was relieved and small negative pressure pulses were applied to achieve GΩ seal formation. Seal resistances were always > 1 GΩ. Recordings were made in current-clamp mode, and no holding current was applied. Typical recording durations were ~15-20 min (which usually allowed 5 minutes recording of baseline and 5-10 minutes after burst trains). Air puff stimulation of the whisker pad was achieved by 1 s-long pulses of compressed air delivered by a picospritzer unit via a 1 mm diameter plastic tube placed at ~20 mm from the mouse snout. To record local field potential (LFP) patch pipette (1-2MΩ) were filled with HEPES-buffered extracellular solution and inserted in the cortex. Data were acquired at 50 kHz using a Multiclamp 700B Amplifier (Molecular Devices).

Biocytin filling

To certify that deep L5 PNs of S1 were being target, experiments were performed in Scnn1a x tdTomato mice allowing labeling of layer 4. Biocytin (Sigma) was added to the intracellular solution at a high concentration (0.5 g / 100 ml). Neurons were injected

with large depolarizing currents in current clamp mode for fifteen times (100 ms, 1-2 nA, 1 Hz). Briefly, after *in vivo* experiments, mice were perfused and brain slices of 200 μm were performed as described above for *in vitro* electrophysiology. Slices were then fixed with 4% paraformaldehyde in phosphate buffer saline (PBS, Sigma) for at least 48 h. Following fixation, slices were incubated with the avidin-biotin complex (VECTASTAIN Elite) and a high concentration of detergent (Triton X-100, 5%) for at least two days before staining with 3,3′Diaminobenzidine (DAB, VECTASTAIN Elite) following (Jiang et al., 2015). Slices were then rinsed in PBS and coverslipped in mounting medium. Immunofluorescence and DAB staining were observed in a Micro Zeiss Routine microscope and images were acquired using a 10-40x objectives.

Analysis of the phase modulation of AP-LFP coupling

The analysis of the coupling between APs and local field potentials (LFP) was done in MATLAB (Mathworks, Natick MA, US), employing custom-written scripts. Briefly, AP occurrence times were extracted from the intracellular membrane potential, recorded and sampled at 50 kHz. This was based on a supervised peak-detection algorithm, using the findpeak() MATLAB function with a −15 mV detection threshold and a 4 ms dead-time. LFP were first down sampled to 1 KHz and then digitally filtered, between 20 and 100 Hz, by a 16^{th} order bandpass Butterworth filter. The waveform was then Hilbert-transformed and its instantaneous phase component unrolled in the range $[0\ ;2\pi\ ]$. For each AP, the corresponding LFP phase was extracted as the corresponding value of the instantaneous phase component. A histogram was used as polar-plot or equivalently as a Cartesian-plot to display the distribution of AP-LFP phases. The confidence interval was estimated by Monte Carlo methods from 100 independent surrogate dataset, obtained upon randomly jittering each AP times (i.e., Gaussian distributed, zero mean, 10 ms standard deviation) and again estimating the distribution of the corresponding LFP phases from the Hilbert instantaneous phase waveform.

Computational model

L5 PNs were modeled as integrate-and-fire neurons, with membrane potential dynamics given by

$$\boldsymbol{c_m}\frac{\boldsymbol{dV}}{\boldsymbol{dt}} = -\boldsymbol{g_m}\boldsymbol{V} + \boldsymbol{I}(\boldsymbol{t})$$

where the membrane potential $\boldsymbol{V}$ is determined with respect to the resting potential of the cell. The membrane capacitance was $\boldsymbol{c_m} =$ 100 pF, and the membrane conductance $\boldsymbol{g} =$ 10 nS. An action potential was emitted when the membrane potential reached a threshold value V_T = 40 mV. The membrane potential was subsequently reset to a value V_R = 0 mV. The total input to the neuron was given by

$$\boldsymbol{I}(\boldsymbol{t}) = \boldsymbol{I_{osc}}(\boldsymbol{t}) + \boldsymbol{I_{bkg}}(\boldsymbol{t})$$

Here I_{osc} represents the oscillatory current received from L2/3 via feed-forward excitation and inhibition. It is therefore given by L2/3 oscillatory activity $r_{2/3}$ (t),

$$\boldsymbol{r}_{2/3}(\boldsymbol{t}) = \boldsymbol{r_f}\boldsymbol{cos}\ (2\pi\boldsymbol{f})$$

filtered by a composite post-synaptic current K(t), modeled as a difference of excitatory and inhibitory components

$$\boldsymbol{K}(\boldsymbol{t}) = \boldsymbol{K_E}\boldsymbol{exp}\left(-\frac{\boldsymbol{t}-\boldsymbol{\delta}_5}{\boldsymbol{\tau_E}}\right)\boldsymbol{\Theta}(\boldsymbol{t}-\boldsymbol{\delta}_5) + \boldsymbol{K_I}\boldsymbol{exp}\left(-\frac{\boldsymbol{t}-\boldsymbol{\delta}-\boldsymbol{\delta}_5}{\boldsymbol{\tau_I}}\right)\boldsymbol{\Theta}(\boldsymbol{t}-\boldsymbol{\delta}-\boldsymbol{\delta}_5)$$

where $\boldsymbol{\tau_E} =$ 2 ms and $\boldsymbol{\tau_I} =$ 7 ms are the timescales of excitation and inhibition, $\boldsymbol{\delta}$ = 2 ms is the delay between excitatory and inhibitory inputs, $\boldsymbol{\delta}_5$ is an overall delay between L2/3 activity and L5 inputs, $\boldsymbol{K_E}$ and $\boldsymbol{K_I}$ represent the strengths of excitation and inhibition, and $\boldsymbol{\Theta}(\boldsymbol{t})$ is the Heaviside step function (0 for t < 0, 1 for t > 1).

The oscillatory input was therefore given by the convolution between K(t) and $\boldsymbol{r}_{2/3}(\boldsymbol{t})$**:**

$$\boldsymbol{I_{osc}}(\boldsymbol{t}) = \int_{-\infty}^{+\infty} \boldsymbol{d\tau}\, \boldsymbol{r}_{2/3}(\boldsymbol{t}-\boldsymbol{\tau})\boldsymbol{K}(\boldsymbol{\tau}).$$

In the simulations, the amplitude of L2/3 oscillations was set to $\boldsymbol{r_f}$ = 3 spk/s, the excitatory strength of the PSC was set to $\boldsymbol{K_E} =$ 20 pA and $\boldsymbol{K_I}$ was varied in the range from 0 to 32 pA, so that oscillations led to composite postsynaptic currents of about 100-350 pA.

Other inputs to the L5 PN were modeled as background noise

$$\boldsymbol{I_{bkg}}(\boldsymbol{t}) = \boldsymbol{\sigma}\sqrt{\boldsymbol{c_m}\boldsymbol{g_m}}\boldsymbol{\xi}(\boldsymbol{t})$$

where $\boldsymbol{\xi}(\boldsymbol{t})$ is Gaussian white noise of zero mean and unit variance, I_0 is the mean input and $\boldsymbol{\sigma}$ is the background noise amplitude. In the simulations in Figure 7 we used $\sigma = 22\ mV$, while in Figure S7 we show the results of simulations for half and double noise amplitude (adjusting the mean input to keep the mean firing rate identical).

The oscillatory input from L2/3 entrains the activity of the L5 PN, which therefore acquires an oscillatory temporal structure. To determine the temporal relationship between L2/3 inputs and the output from L5PNs, we computed the trial-averaged firing rate $r_5(t)$ (histograms in Figure 7C bottom). If the oscillatory inputs are relatively weak, L5 PN activity can be approximated as

$$r_5(t) = r_5^{(0)} + r_5^{(1)} cos\ (2\pi - \phi)$$

where the first term represents constant activity, and the second term describes an oscillation around that baseline. The phase ϕ quantifies the timing of the output with respect to the L2/3 oscillatory input, while the amplitude $r_5^{(1)}$ quantifies the precision of this timing – the larger $r_5^{(1)}$, the more L5 PN action potentials are concentrated at the specific phase of the input given by ϕ.

Our aim was to understand how the shape of the composite post-synaptic current K(t) influences the timing and precision of the L5 PN output. Previous theoretical works (for a review, see Brunel and Hakim, 2008) showed that for weak inputs the phase and amplitude of the output can be decomposed into a synaptic and a neuronal contribution:

$$\phi = \phi_{syn} + \phi_n$$

$$r_5^{(1)} = A_{syn} A_n.$$

Here the neuronal contributions ϕ_n and A_n to the phase and amplitude depend on the background noise input and the specific neural model (Brunel et al., 2001; Fourcaud-Trocmé et al., 2003). As we did not vary the background noise parameters, we treated them as arbitrary constants.

The synaptic phase lag ϕ_{syn} and amplitude A_{syn} are given by the phase and amplitude of the Fourier transform $\tilde{K}(f)$ of the Fourier transform of the composite post-synaptic current K(t):

$$\tilde{K}(f) = \frac{e^{-2\pi i f \delta_5}}{\sqrt{2\pi}} \left(\frac{K_E \tau_E}{2\pi i f \tau_E + 1} - \frac{K_I \tau_I}{2\pi i f \tau_I + 1} e^{-2\pi i f \delta} \right).$$

The phase and amplitude of $\tilde{K}(f)$ depend on the frequency of the oscillation (as well as on synaptic parameters). Since we were looking at the response to L2/3 inputs oscillating at 30Hz, $\tilde{K}(f)$ was evaluated at f = 30 Hz, and a range of K_I/K_E values was used (see Figure 7). The phase and the amplitude of the obtained values were then compared with direct fits of a cosine function to simulation results (Figure 7). Note that the above theoretical prediction for the phase and amplitude of L5 PN output rely on a linear approximation, expected to be accurate if the amplitude of the oscillations is not too strong. The comparison between the prediction and simulations indeed shows deviations from the predicted amplitude when inhibition becomes very strong (Figure 7E).

QUANTIFICATION AND STATISTICAL ANALYSIS

Analysis of LTP was performed by comparing the mean amplitude of light evoked inhibitory postsynaptic currents in the 5 last minutes of the plasticity to the baseline period (Figure 1). Unless otherwise indicated, statistical comparisons were done between raw values.

Normality of the data was assessed (D'Agostino & Pearson omnibus normality test). Normal distributions were statistically compared using paired t test two-tailed and Wilcoxon matched-pairs signed rank test was used as a non-parametric test. Group data was analyzed using the either Friedman test followed by Dunn's multiple comparison test when comparing repeated-measurements (e.g., Figure 2D for different frequencies and Figure 3D), or Kruskal-Wallis Test (e.g., Figure 4F). Differences were considered significant if $p < 0.05$. Values are presented as mean ± SEM of *n* experiments.

Gain modulation (Figure 2F) was calculated from the average slope (F′) of the fits between 5% and 75% of its maximum value (Rothman et al., 2009). Only cells where the fit was possible were included in the calculation. Changes in gain (ΔGain) were computed as follows:

$$\Delta Gain = \frac{\left(F'\,\mathrm{LTPi} - F'\,\mathrm{bsl} \right)}{F'\ \mathrm{bsl}} \times 100.$$

Additive offset shifts (ΔOffset) were defined as the difference between the half-maximum frequencies of the fits for the two conditions LTPi and baseline.

DATA AND CODE AVAILABILITY

The code used to generate the model in Figures 7 and S7 is available at https://github.com/MathildeBigot. All the other scripts supporting this study have not been deposited in a public repository, because they are standard analysis routines. However, they are available from the corresponding author upon request. The source datasets is available in Mendeley Data (https://data.mendeley.com/datasets/75t97ncb24/2).